Evolution of H2O content in deforming quartz aggregates: An experimental study

H Stünitz, Hugues Raimbourg, L Nègre, J Précigout, M Jollands, P Pongrac, P Jeřabek, N Gies, M Lüder

Journal of Structural Geology 178 (2024) 105029

Contents lists available at ScienceDirect

Journal of Structural Geology

journal homepage: www.elsevier.com/locate/jsg

Evolution of H_2O content in deforming quartz aggregates: An experimental study

H. Stünitz [a,b,*], H. Raimbourg [a], L. Nègre [a], J. Précigout [a], M. Jollands [c], P. Pongrac [d], P. Jeřabek [d], N. Gies [e], M. Lüder [e]

[a] Institut des Sciences de la Terre d'Orléans (ISTO), Université d'Orléans, 1A, rue de la Ferollerie, 45100, Orléans, France
[b] Department of Geosciences, University of Tromsø, Dramsveien 201, 9037, Tromsø, Norway
[c] Gemological Institute of America, 50 W 47th Street, New York, NY, 10036, USA
[d] Institute of Petrology and Structural Geology, Faculty of Science, Charles University, Albertov 6, Praha 2, CZ-128 43, Czech Republic
[e] Institute of Geological Sciences, Universität Bern, Baltzerstrasse 1+3, CH-3012, Bern, Switzerland

A B S T R A C T

Deformation experiments were carried out on pure quartzite samples (>99% quartz) with a grain size of ~200 μm from Tana, Northern Norway. Deformation conditions were 900 °C, 0.1 wt% H_2O added, strain rate ~1×10^{-6} s^{-1} at variable confining pressures from 600 to 2000 MPa. Detailed FTIR measurements of H_2O indicate that the H_2O content in the grain boundary region is higher than that inside quartz grains. Hydrostatic treatment and deformation at the chosen temperature and pressure conditions lead to further H_2O loss from grain interiors and H_2O increase in the grain boundary region. Varying the confining pressure does not have an observable effect on the H_2O transfer from grains to the grain boundary region. The 3585 cm^{-1} absorption band increases systematically with increasing confining pressure. As this band is associated with OH in dislocations, the increase may indicate an increased dislocation density with increasing pressure. The triplet of 3317, 3375 and 3438 cm^{-1} associated with Al-content in quartz increases in the grain boundary region indicating an exchange of H^+ together with Al^{3+} for Si^{4+}. The Al and H exchange suggest dissolution-precipitation processes in the grain boundary region facilitating the movement of the quartz grain boundaries (grain boundary migration). The H_2O in the grain boundary region will be important for enhancing grain boundary migration and thus recrystallization processes during deformation.

1. Introduction

Since the early experiments by Griggs and Blacic (1965) it has been demonstrated in numerous studies that H_2O has a pronounced weakening effect on the plastic deformation of quartz and other silicates (e.g., Griggs 1967; Blacic 1975; Tullis and Yund 1980), and it is the commonly accepted view that deformation of silicates in the crust and upper mantle is facilitated by small amounts of H or H_2O. The active processes of weakening may be different in different minerals (e.g., FitzGerald et al., 1991; Mei and Kohlstedt 2000; Rybacki and Dresen 2000; Dimanov and Dresen 2005). For quartz, it has been demonstrated that the weakening agent is molecular H_2O, not H-point-defects (Kekulawala et al., 1981; Paterson 1989; Kronenberg 1994; Cordier et al., 1994). The solubility of H_2O in quartz is negligibly small (e.g., Paterson 1986, 1989; Kronenberg et al., 2017), so that H_2O usually is present as fluid inclusions (e.g., Kekulawala et al., 1981; Paterson 1989; Tarantola et al., 2010). The size of these inclusions can be extremely variable, from hundreds of micrometers down to the nm-scale (Kekulawala et al., 1981; Aines et al., 1984; McLaren et al., 1989; Tarantola et al., 2010, 2012).

As the solubility of H_2O in quartz is very low, H_2O needs to be transported into the grains. The transport of H_2O into quartz typically takes place by advective processes through microcracks, not by diffusion (Kronenberg et al., 1986; Gerretsen et al., 1989). The microcracking and crack healing can easily generate fluid inclusions as well as glissile dislocations in quartz, so that this process is important for facilitating crystal plastic deformation (McLaren et al., 1989; FitzGerald et al., 1991; Tarantola et al., 2010, 2012, Stünitz et al., 2017). Removal of H_2O from interiors of grains can be facilitated by grain boundary migration (e.g., Kilian et al., 2016) or other means such as micro-cracking (Palazzin et al., 2018) or involving dislocations (Kronenberg et al., 2017, 2020). Thus, microcracking, crack healing, grain boundary migration and other advective processes appear to transfer H_2O between quartz crystals and a H_2O reservoir during deformation. The interplay of different processes is important to understand the H_2O budget in quartz aggregates and its role for crystal plastic deformation processes. In order to study the parameters controlling these processes, deformation experiments have been carried out on very pure quartzite samples. As confining pressure is of major importance for the effect of H_2O on deformation (e.g., Kronenberg and Tullis 1984), experiments have been performed at different confining pressures. The H_2O content has been determined post mortem

* Corresponding author. Institut des Sciences de la Terre d'Orléans (ISTO), Université d'Orléans, 1A, rue de la Ferollerie, 45100, Orléans, France.

https://doi.org/10.1016/j.jsg.2023.105029
Received 6 June 2023; Received in revised form 29 November 2023; Accepted 29 November 2023
Available online 10 December 2023

by Fourier transform infrared spectroscopy (FTIR).

2. Material, experiments, and analytical methods

2.1. Starting material

The material used in this study is a natural quartzite, called Tana quartzite, from the ELKEM quarry in Austertana, Northern Norway (N70°28′39.6'', E28°32′30.1''; for details see Négre et al. (2021) and Pongrac et al. (2022)). The Tana quartzite is used by the aluminium, silicon, and ferrosilicon industry (Aasly et al., 2007) because of its purity (>99% silica). Chemical analyses (from ICP-EOS) published in Pevik (2015) indicate major oxide values (apart from SiO_2) of 3547 ± 1083 ppm Al_2O_3, 441 ± 365 ppm Fe_2O_3, and 207 ± 37 ppm TiO_2.

The Tana quartzite underwent high grade diagenesis to very low grade metamorphism. The quartzite is composed of quartz sand grains and crystalline authigenic SiO_2 cement (99%, Fig. 1a and b) and very few accessory minerals (<1%) such as white micas (sericite, pyrophyllite), iron oxides (hematite), zircons, and very rare feldspars. Due to filling of the pore space by authigenic SiO_2 cement, no visible porosity was detected in the light microscope or SEM (Fig. 1).

Microstructural analysis and CL-imaging show that the quartz grains forming the Tana quartzite are composed of cores of equant and rounded detrital quartz sand grains, with various CL-colours and -intensity, and a non- or dark-luminescent cement between the grains (Fig. 1c and d). The cement is in crystallographic continuity with the sand grains on which it grows (Fig. 1a). Grains appear undeformed as they do not show undulatory extinction, except for rare sand grains showing inherited recrystallized microstructures. Occasionally, a few pressure-solution contacts due to burial of the sediment are observed.

The size distribution of quartz grains composing the quartzite was obtained by image analysis using both polarized light and light microscopy (LM)-CL-images. The mean grain size is 204 μm for quartz grains and 186 μm for original sand grains (Négre et al., 2021).

2.2. Deformation experiments

2.2.1. Experimental conditions

All details regarding deformation experiments are provided in Négre et al. (2021), only a brief summary is given here. Coaxial shortening experiments of cylindrical cores of the Tana quartzite have been performed in a new generation solid medium Griggs-type apparatus, with NaCl as the confining medium (Précigout et al., 2018). A first series of experiments has been performed to approximately 30 % coaxial shortening (total strain of samples is between ~26 and 33 %) at a temperature of 900 °C and constant strain rate of approximatively 10^{-6} s^{-1}, with variable confining pressures (600, 700, 800, 1000, 1250, 1500 and 2000 MPa) (Table 1). In all experiments, 0.1 wt% of H_2O has been added to the assemblage prior to deformation. A second series of experiments has been carried out at 2000 MPa, 900 °C and a strain rate in the range of ~10^{-5} s^{-1} to ~10^{-6} s^{-1}, with a variable amount of finite strain up to ~40%. One sample (OR56) was deformed at 2000 MPa at a faster strain rate of ~ 10^{-5} s^{-1} and shortened by 70%. Two additional hydrostatic experiments have been carried out at 1000 and 2000 MPa, 900 °C, only

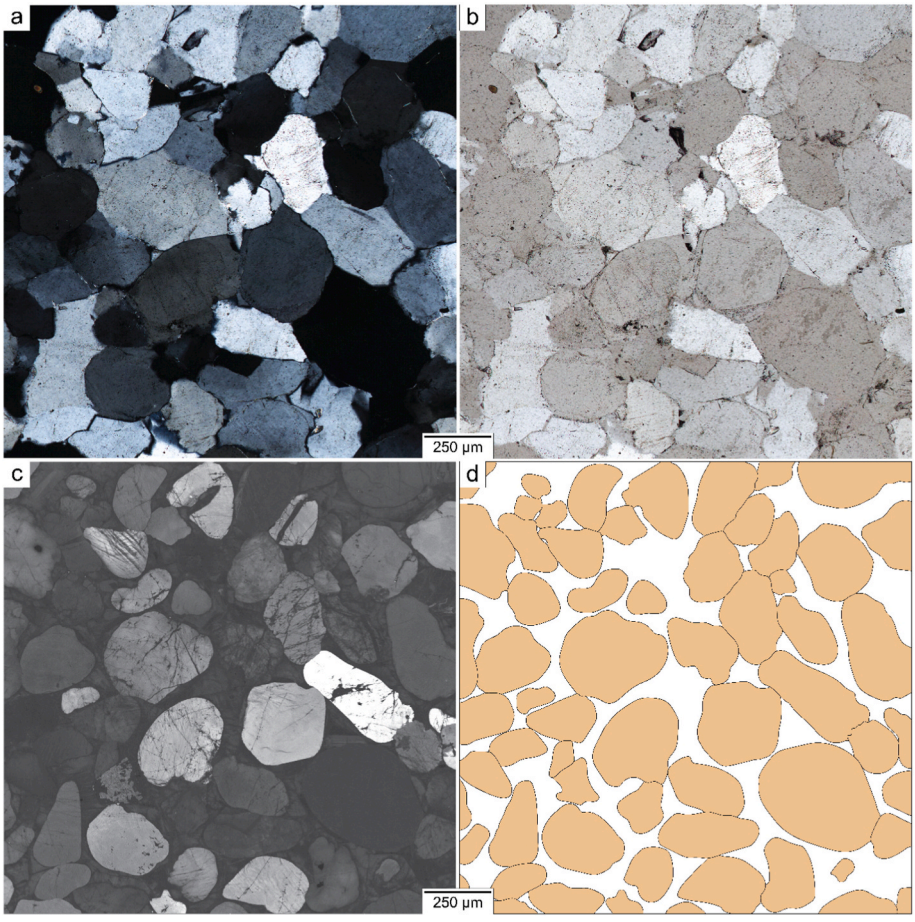

Fig. 1. Starting material of Tana quartzite. (a) Light microscope cross polarized image. (b) light microscopy plane polarized image. Fluid inclusion arrays are observable in some grains. (c) SEM-cathodoluminescence image, (d) sketch of segmented detrital sand grains (beige) with the surrounding cement (white). The quartzite crystals are composed of detrital sand grains and cement that grows with the same crystal orientation on the sand grains. (For interpretation of the references to colour in this figure legend, the reader is referred to the web version of this article.)

Table 1
List of conditions for experiments at constant displacement rate. Strain rate stepping experiments are not listed here.

Sample name	Griggs apparatus	Temperature (°C)	Water added (wt. %)	Confining pressure (MPa)	Strain rate (s^{-1})	Shortening calculated (%)	Shortening measured (%)
542LN	Tromsø	900	0.1	600	1.29E-06	33.46	30.48
544LN				1500	1.37E-06	33.48	30.71
546LN				1000	1.28E-06	31.27	28.01
OR32	Orléans			1000	9.32E-07	30.96	29.39
OR33				800	9.20E-07	24.35	23.30
OR42				800	8.12E-07	29.71	30.83
OR48				1250	8.80E-07	28.42	27.71
OR50				2000	~9E-07	~43	52.38
OR52				700	8.26E-07	31.98	32.12
OR54				2000	~9E-07	~29	39.75
OR56				2000	~9E-06	~70	74.43
OR57				2000	~9E-07	~23	27.76
OR60				600	7.33E-07	30.92	30.57
OR62				2000	9.29E-07	30.53	29.51
OR63				1500	~9E-07	~25	25.31
OR64				1500	9.40E-07	29.76	26.59
OR59				1000	Hydrostatic (251.7 h)		0.53
OR66				2000	Hydrostatic (216.8 h)		–
OR73			0	800	7.68E-07	31.66	29.02

temperature and the confining pressure were applied without deformation. The duration of the hydrostatic experiments was chosen to be identical to the total time at which the samples of the deformation experiments were exposed to pressure and temperature. The duration of the hydrostatic experiments was between 217 and 252 h, so that all samples were kept at pressure and temperature between approximately 200 and 260 h. Mechanical results and microstructures of these experiments are available in a previous publication (Négre et al., 2021).

2.2.2. *Samples and microstructures after deformation*

The local strain distribution in all samples is inhomogeneous. Typically, the centre and/or bottom parts of the samples are more strongly deformed, while the top part of the samples, especially near the alumina piston, is less deformed.

As was demonstrated by CL-imaging of the original sand grains and their variations in shape with strain, crystal plastic deformation of the individual quartz grains is the dominant process accommodating the deformation (Négre et al., 2021). In addition, processes of recrystallization, highlighted by a bright blue luminescence, are present

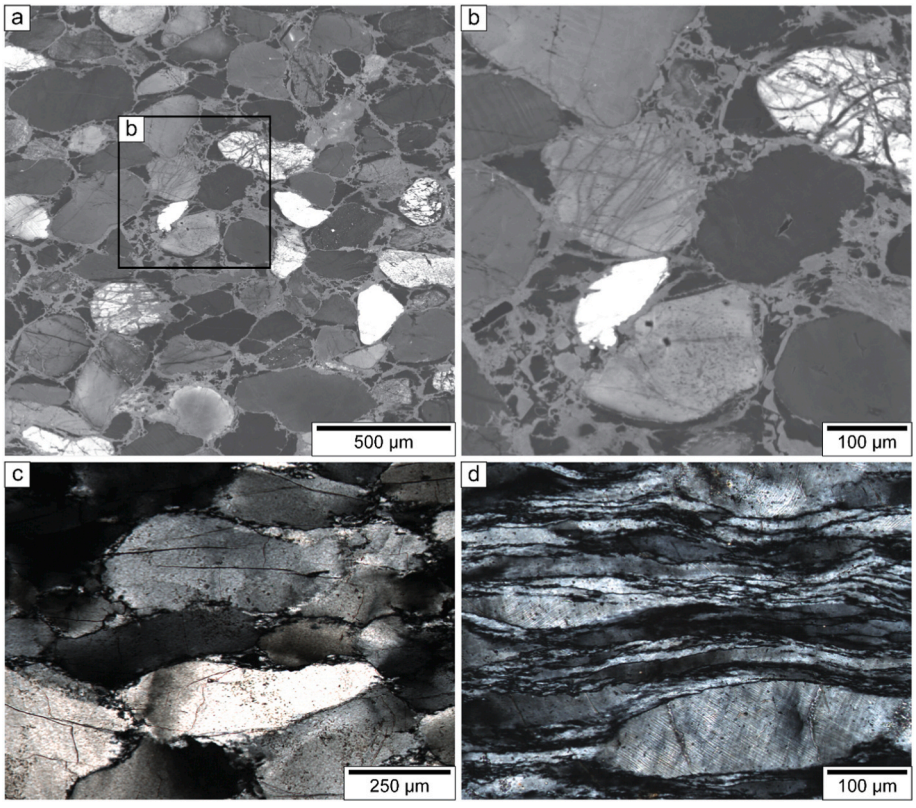

Fig. 2. (a & b) SEM-CL images from sample OR64 deformed at 1500 MPa confining pressure. Bright luminescence highlights cracking and recrystallized regions (medium grey level). Larger fragments show the original luminescence. (c & d) Light microscope crossed polarized images of (c) elongated grains from sample OR32 (1000 MPa) with recrystallized regions along the grain boundaries and (d) elongated grains and deformation lamellae from high-strained sample OR56 (2000 MPa). The shortening direction is vertical for all images.

principally along the grain boundaries and in cracks. Recrystallization becomes more abundant with increasing confining pressure and is accommodated by two different mechanisms: (1) subgrain rotation in the plastically deformed original quartz grains, and (2) local grain boundary migration accommodated by dissolution-precipitation of quartz (Fig. 2 a and b). Nuclei for new grains modified by grain boundary migration often are small fragments originated by cracking concentrated near the grain boundaries (Négre et al., 2021; Pongrac et al., 2022).

2.3. H_2O measurements

Double-polished thick sections with thicknesses between 80 and 230 μm have been prepared from the starting material and deformed samples. Fourier transform infrared spectroscopy (FTIR) analysis has been performed at ISTO (Orléans) with a Nicolet 6700 (Continuμm, Thermo Scientific) spectrometer and OMNIC (version 8) acquisition software.

The spectra were acquired with 64 or 128 scans and a resolution of 4 cm^{-1} for a range of wavenumbers from 5500 to 1500 cm^{-1}. The measurements have been made on grain interiors (centre of grains) and on grain boundaries (at the junction between two grains). For some samples deformed at 2000 MPa, measurements were also made on regions showing small grains (recrystallized/cracked material). A window with 40 × 40 μm for interior of grains and with 20 × 50 μm was used for grain boundary measurements (window shape and orientation were adapted to the boundaries). The background was recorded for the CaF_2 window carrying the sample and subtracted from the measured spectra.

Baseline correction (between 5500 and 1500 cm^{-1}) and correction for Araldite®: The spectra were corrected for a flat baseline and for eventual presence of water due to Araldite®.

Following the procedure described in Sambridge et al. (2008) for unpolarized FTIR measurements, the total absorbance (A_{total}), can be estimated from the average of absorbance measurements using unpolarized light over a large number of grains randomly orientated and contained within the thick section (A_{unp}^{avg}), as $A_{tot} = 3A_{unp}^{avg}$. The conversion from total absorbance to concentration c_{H_2O} was carried out using the using the Beer-Lambert law as $c_{H_2O} = \frac{A_{tot}}{\varepsilon \cdot t}$, where t is the thickness and ε is the integrated molar absorption coefficient. For the latter, we used the values estimated by Thomas et al. (2009) as $\varepsilon = 89,000 \pm 15,000 L.mol^{-1}cm^{-2}$, also used in the review by Stalder (2021). Please note that several calibrations exist to convert absorbance into concentrations, which were reviewed in Fukuda and Shimizu (2019). Another point of caution, in the conversion, is the use of either absorbance measured in a single section of the mineral, or total absorbance, measured on three mutually orthogonal section planes (or equivalently from the average over many randomly orientated grains with the same water content, as detailed above). For example, from the widely used Paterson (1982) calibration Fukuda and Shimizu (2019) estimated an integrated molar absorption coefficient $\varepsilon = 38,000 L.mol^{-1}cm^{-2}$, which applies to absorbance measured in a single section plane of the mineral. Considering total absorbance and assuming isotropic absorption, the corresponding integrated molar absorption coefficient is therefore $38,000 \times 3 = 114,000 L.mol^{-1}cm^{-2}$, hence relatively close to the value used in the present work. Given all these conditions and limitations of H-measurements, the quantification of H_2O should be considered semi-quantitatively, i.e., absolute numbers are given for relative comparison.

In the following, the water contents will be presented in molar proportions of H atoms per 10^6 Si atoms ($H/10^6$ Si). A summary of FTIR measurements is given in Table 2, while all measurements are given in the Appendix. Error bars were calculated as the standard deviation over all FTIR measurements for a given sample and microstructure (the number of measurements is given in Table 2). Please note that in a few cases, due to a few grains very rich in water, the standard deviation is larger than the average value of the distribution.

Transmission FTIR mapping was carried out at the Institute of Geological Sciences of the University of Bern using a Bruker Tensor II spectrometer with a globar infrared source and a KBr beam-splitter, coupled to a Bruker Hyperion 3000 microscope with a dry air-purged sample chamber. The instrument is equipped with a focal plane array (FPA) detector with 64 × 64 = 4096 liquid-nitrogen-cooled MCT elements on a square array with a pixel size of 2.7 μm × 2.7 μm. A 2 × 2 binning was used resulting in a 5.4 × 5.4 μm pixel resolution, higher signal quality and an improved signal to noise ratio. Spectra were acquired with 8 cm^{-1} wavenumber resolution and 128 scans between 900 and 3850 cm^{-1}.

For the data processing of the FTIR-FPA maps the atmospheric correction and concave rubber band correction with 64 points and four iterations were performed in OPUS® version 8.5. The spectra were then exported and further processed with the in-house developed MATLAB software SpecXY (Gies et al., 2023). The spectra were normalized to 1 cm thickness and integrated absorbance for different maps were generated by extracting the chosen part of the signal, performing a linear baseline correction between the integration endpoints, and integrating the corrected spectra.

2.3.1. Epoxy correction

Inadvertently, Araldite® epoxy (instead of H_2O-free wax) was used for sample impregnation during the thick section preparation. As some H_2O is contained in the epoxy, the FTIR spectra need to be corrected for this additional H_2O content in the 3000–3800 cm^{-1} absorption band range. The Araldite® epoxy shows CH absorption bands in the 2600–3100 cm^{-1} region (with two principal peaks at ~2931 and 2869 cm^{-1}), which are unique to this epoxy and absent in quartz and H_2O spectra. Pure Araldite® samples of different thickness have been prepared and measured with FTIR using the same settings as during samples measurements. In order to obtain a correction routine, the H_2O broad band of the Araldite® has been related to the two discrete bands unique to Araldite. The correction uses the epoxy CH-bands and their associated H_2O concentration to subtract the additional H_2O content arising from the Araldite®. The correction has been applied to all spectra that show detectable Araldite® discrete absorption bands but only to individual spectra and not to the maps shown in Figs. 5 and 6.

3. Results of H_2O measurements

3.1. Starting material: variations in H_2O content for grain interiors and grain boundary regions

Grain interiors have systematically lower mean H_2O contents than all other measurements including grain boundary regions: Grain boundary regions between two grains, triple junctions, and cement. Due to the small size of the domains of cement, it is very likely that those measurements also integrate a contribution of H_2O in the grain boundary region (Fig. 3a).

3.2. Effect of P-T-strain application on H_2O content

All samples that have been deformed or treated hydrostatically at high pressure and temperature show H_2O contents that are significantly lower than that of the starting material (Fig. 3b). The comparison between the hydrostatically treated sample (mean value for grain interiors) and the deformed samples (including low strain and high strain areas) indicates that the hydrostatic application of pressure and temperature produces an initial and major decrease in the H_2O content, while deformation continues to decrease it further, but to a smaller extent (Fig. 3b).

3.3. Effect of pressure on H_2O content

There appears to be no systematic effect of the confining pressure

Table 2
Summary of FTIR measurements for all samples.

Sample name	Pressure in GPa (for deformation expts); experimental conditions or type of material	Microstructure	Epoxy organics, total integrated absorbance (cm^{-2})	Standard deviation	AlH total integrated absorbance (cm^{-2})	Standard deviation	H_2O broad total integrated absorbance (cm^{-2})	Standard deviation	Band at 3627 cm^{-1}, total integrated absorbance (cm^{-2}) (assume isotropic)	Standard deviation	Band at 3585 cm^{-1}, total integrated absorbance (cm^{-2})	Standard deviation	Band at 3700 cm^{-1}, total integrated absorbance (cm^{-2}) (assume isotropic)	Standard deviation	Number of measurements	Water concentration in quartz (H/10^6 Si)	Uncertainty (H/10^6 Si)
542LN	0.6	Grain interior (low strain)	174.23	124.92	171.32	105.81	3648.20	2728.97	134.38	109.35	4.35	3.67	6.08	7.83	87.00	1915.31	1432.71
		Grain boundary (low strain)	259.34	170.03	278.47	187.07	4233.56	2873.92	152.27	136.78	5.05	4.04	3.47	3.66	61.00	2222.62	1508.81
		Grain interior (high strain)	102.26	66.38	157.86	107.39	3022.77	2028.56	88.73	57.68	5.32	3.85	0.77	1.94	60.00	1586.96	1064.99
544LN	1.5	Grain interior (low strain)	126.21	111.29	176.90	93.49	5622.60	5229.51	263.24	250.42	22.14	7.41	3.49	4.51	135.00	2951.86	2745.49
		Grain boundary (low strain)	333.00	270.94	299.57	142.47	6150.04	3366.62	779.61	878.33	17.58	9.65	2.98	4.79	64.00	3228.77	1767.47
		Grain interior (high strain)	148.60	83.99	213.81	139.92	2833.42	2390.87	93.03	111.30	21.01	5.92	6.16	5.81	64.00	1487.55	1255.21
		Grain boundary (high strain)	267.27	295.45	292.36	141.27	5303.58	3892.83	169.78	166.43	17.89	6.41	2.85	5.12	69.00	2784.38	2043.74
546LN	1	Grain interior (low strain)	106.34	112.39	193.06	94.77	6606.64	3828.19	166.32	113.46	12.29	5.60	3.54	6.82	94.00	3468.49	2009.80
		Grain boundary (low strain)	173.17	118.65	283.30	125.15	6884.39	2730.74	204.73	122.11	13.04	5.32	7.36	8.26	70.00	3614.30	1433.64
		Grain interior (high strain)	160.64	187.93	200.60	119.65	3459.54	2705.12	99.80	97.23	17.22	6.33	3.74	4.94	134.00	1816.26	1420.19
		Grain boundary (high strain)	342.88	312.86	324.54	190.22	5151.65	3485.07	129.06	102.31	12.94	5.49	6.23	6.63	67.00	2704.62	1829.66
OR32	1	Grain interior (low strain)	984.93	1040.78	236.65	132.76	3029.17	2273.34	61.94	61.10	12.45	5.30	1.31	2.59	74.00	1590.31	1193.51
		Grain boundary (low strain)	2126.55	1589.71	327.13	148.68	4054.62	2894.27	79.94	96.47	12.34	5.40	3.34	4.27	63.00	2128.68	1519.49
		Grain interior (high strain)	1089.66	1300.14	197.46	138.08	2963.88	2166.37	103.89	91.25	15.27	4.50	4.48	9.46	32.00	1556.04	1137.34
		Grain boundary (high strain)	1719.82	1557.35	342.38	191.87	3043.22	2492.98	41.57	69.55	13.34	5.10	2.85	3.53	34.00	1597.69	1308.81
OR33	0.8	Grain interior (low strain)	1623.27	1617.00	231.02	159.95	4077.97	2501.38	73.57	75.86	9.37	3.59	2.16	4.02	50.00	2140.94	1313.23
		Grain boundary (low strain)	2902.95	1902.33	325.36	132.09	5917.62	3338.49	137.31	163.60	10.41	3.84	2.94	8.64	50.00	3106.75	1752.71
		Grain interior (high strain)	1275.79	1057.02	208.98	116.31	3366.31	1481.65	92.87	92.96	10.50	3.57	2.66	6.70	34.00	1767.31	777.86
		Grain boundary (high strain)	2274.55	1670.99	320.70	161.90	4489.18	2041.43	68.17	63.51	9.81	3.64	1.28	2.00	49.00	2356.82	1071.75

(*continued on next page*)

Table 2 (*continued*)

Sample name	Pressure in GPa (for deformation expts); experimental conditions or type of material	Microstructure	Epoxy organics, total integrated absorbance (cm^{-2})	Standard deviation	AlH total integrated absorbance (cm^{-2})	Standard deviation	H_2O broad total integrated absorbance (cm^{-2})	Standard deviation	Band at 3627 cm^{-1}, total integrated absorbance (cm^{-2}) (assume isotropic)	Standard deviation	Band at 3585 cm^{-1}, total integrated absorbance (cm^{-2})	Standard deviation	Band at 3700 cm^{-1}, total integrated absorbance (cm^{-2}) (assume isotropic)	Standard deviation	Number of measurements	Water concentration in quartz (H/10^6 Si)	Uncertainty (H/10^6 Si)
OR42	0.8	Grain interior (low strain)	799.59	1489.56	186.40	102.50	4903.01	3361.52	63.77	63.80	8.57	4.69	2.23	3.02	44.00	2574.08	1764.80
		Grain boundary (low strain)	1910.62	1847.08	261.93	111.90	5131.90	2919.14	66.87	68.76	5.76	3.80	1.69	2.92	47.00	2694.25	1532.55
		Grain interior (high strain)	768.66	851.95	168.51	79.71	1843.13	974.06	28.71	25.76	6.41	3.54	0.66	1.28	36.00	967.65	511.38
		Grain boundary (high strain)	1925.13	1350.66	258.39	134.38	4485.86	3826.82	156.94	192.30	8.46	5.94	1.06	3.68	31.00	2355.08	2009.08
OR48	1.25	Grain interior (low strain)	525.48	711.04	233.59	136.79	2346.62	1460.47	51.12	54.48	13.80	4.95	5.95	6.04	48.00	1231.98	766.75
		Grain boundary (low strain)	1500.66	1077.88	346.04	156.97	4699.58	5059.77	119.55	228.14	13.36	4.77	4.93	10.27	52.00	2467.28	2656.38
		Grain interior (high strain)	420.26	449.96	168.68	86.81	2295.97	1620.96	100.72	112.10	14.83	4.52	3.73	5.30	33.00	1205.38	851.00
		Grain boundary (high strain)	1042.66	804.53	299.83	86.84	2870.38	1571.54	60.79	77.45	14.17	4.13	2.17	3.02	49.00	1506.95	825.06
OR50	2	Grain interior (low strain)	208.04	126.14	172.33	83.33	2600.19	2067.13	98.37	148.86	22.69	7.04	5.65	16.46	51.00	1365.10	1085.24
		Grain boundary (low strain)	377.51	516.95	288.61	116.71	2257.32	2150.94	79.36	114.71	16.21	6.21	2.89	3.74	53.00	1185.09	1129.24
		Grain interior (high strain)	148.13	74.76	176.15	77.31	1315.81	1036.35	43.83	62.13	26.81	6.41	3.16	3.61	46.00	690.80	544.08
		Grains recrystallized	333.40	380.77	246.65	93.50	4484.55	3659.79	175.95	187.56	19.24	4.45	5.82	8.99	70.00	2354.39	1921.39
OR52	0.7	Grain interior (low strain)	980.17	1216.90	234.14	146.24	4707.61	3059.74	82.71	97.06	7.37	4.02	2.29	3.23	60.00	2471.49	1606.36
		Grain boundary (low strain)	1899.63	1639.92	313.43	171.45	5318.98	3472.37	124.48	134.43	6.35	4.12	0.78	1.26	55.00	2792.47	1822.99
		Grain interior (high strain)	929.61	880.23	170.97	111.68	2888.61	1512.47	76.71	72.89	5.54	3.80	1.49	2.31	40.00	1516.52	794.04
		Grain boundary (high strain)	2456.72	2096.97	314.54	137.20	4769.92	3378.02	151.37	136.95	5.08	4.68	2.25	3.16	36.00	2504.21	1773.46
OR54	2	Grain interior (low strain)	208.74	99.65	228.41	167.80	3184.52	2545.77	124.43	128.63	29.95	10.48	8.33	8.14	36.00	1671.87	1336.53
		Grain boundary (low strain)	589.59	630.20	285.15	111.88	3530.51	1761.27	92.69	89.67	20.64	6.57	2.82	4.11	60.00	1853.52	924.67
		Grain interior (high strain)	89.49	134.23	218.12	94.03	2599.53	1643.07	113.76	93.32	36.04	6.66	17.54	22.53	49.00	1364.75	862.61
		Recrystallized grains	293.03	254.61	306.99	129.42	2949.86	2734.35	168.10	174.37	23.79	6.92	3.52	4.58	67.00	1548.67	1435.54

(*continued on next page*)

Table 2 (*continued*)

Sample name	Pressure in GPa (for deformation expts); experimental conditions or type of material	Microstructure	Epoxy organics, total integrated absorbance (cm^{-2})	Standard deviation	AlH total integrated absorbance (cm^{-2})	Standard deviation	H_2O broad total integrated absorbance (cm^{-2})	Standard deviation	Band at 3627 cm^{-1}, total integrated absorbance (cm^{-2}) (assume isotropic)	Standard deviation	Band at 3585 cm^{-1}, total integrated absorbance (cm^{-2})	Standard deviation	Band at 3700 cm^{-1}, total integrated absorbance (cm^{-2}) (assume isotropic)	Standard deviation	Number of measure ments	Water concentration in quartz (H/10^6 Si)	Uncertainty (H/10^6 Si)
OR56	2	Grain interior (low strain)	436.21	541.20	226.44	82.42	4348.66	2041.18	120.89	107.78	36.27	10.85	7.39	9.90	23.00	2283.05	1071.62
		Grain boundary (low strain)	877.19	973.84	290.82	102.54	5406.59	2371.91	107.00	115.03	30.76	11.01	4.75	6.06	30.00	2838.46	1245.25
		Grain interior (high strain)	136.15	129.04	293.29	107.90	4568.21	2182.30	183.92	190.57	34.59	10.02	22.40	24.88	20.00	2398.31	1145.71
		Very deformed cement	158.39	203.99	356.44	118.33	4175.25	1833.62	83.15	102.00	25.50	8.61	3.32	7.24	37.00	2192.01	962.65
OR57	2	Grain interior (low strain)	133.97	117.10	159.09	79.71	4338.68	3120.11	150.89	126.45	21.77	7.27	3.07	6.05	49.00	2277.81	1638.06
		Grain boundary (low strain)	264.10	358.22	221.93	90.22	5867.64	4643.60	245.37	177.55	21.00	6.05	5.28	6.27	68.00	3080.51	2437.89
		Grain interior (high strain)	81.06	92.15	159.90	72.00	3144.10	2219.16	189.34	136.19	34.96	9.49	37.95	34.40	32.00	1650.65	1165.06
		Grain boundary (high strain)	147.12	143.93	253.71	91.60	3029.01	1465.87	99.68	76.05	24.32	5.79	4.68	4.32	40.00	1590.23	769.58
		Recrystallized grains	276.70	276.65	198.13	84.40	5727.70	2908.35	332.39	184.77	27.99	6.84	4.19	4.68	29.00	3007.04	1526.89
OR59	1; hydrostatic expt	Grain interior	1234.83	1326.09	261.81	139.20	5478.81	3075.98	145.56	113.88	21.97	5.27	6.89	6.09	58.00	2876.38	1614.89
		Grain boundary	3336.33	1845.00	397.17	187.68	10448.85	5141.83	357.31	244.12	19.31	5.70	2.53	4.19	68.00	5485.64	2699.46
OR60	0.6	Grain interior (low strain)	2930.36	2082.23	221.16	128.76	6112.53	5843.71	191.88	299.57	5.92	5.73	1.52	3.47	29.00	3209.08	3067.95
		Grain boundary (low strain)	5899.04	2413.63	357.87	207.37	12474.96	9768.41	545.41	732.29	11.07	7.81	6.71	22.01	19.00	6549.36	5128.41
		Grain interior (high strain)	2095.42	1780.76	217.51	133.82	5360.73	5608.30	219.35	396.62	4.90	5.00	1.60	4.21	33.00	2814.38	2944.36
		Grain boundary (high strain)	6086.25	2946.90	401.22	270.81	13460.68	11765.41	709.62	931.64	6.54	6.54	9.15	24.69	26.00	7066.86	6176.84
OR62	2	Grain interior (low strain)	203.77	231.41	204.01	76.16	3995.72	2456.75	203.42	201.00	21.21	8.39	1.72	3.73	35.00	2097.75	1289.79
		Grain boundary (low strain)	312.73	449.32	218.24	81.63	4206.29	1861.41	274.59	243.03	19.42	6.69	3.43	5.26	65.00	2208.30	977.24
		Grain interior (high strain)	148.56	132.46	197.75	87.22	3313.62	2105.63	122.61	136.92	29.07	7.60	4.45	6.01	29.00	1739.65	1105.46
		Grain boundary (high strain)	246.68	197.00	255.60	66.62	3902.21	2621.51	227.64	269.41	26.49	10.57	5.01	10.46	47.00	2048.66	1376.29
OR63	1.5	Grain interior (low strain)	138.73	59.18	194.08	82.07	2472.39	1625.07	226.15	340.43	12.72	4.55	16.31	20.66	31.00	1298.00	853.16
		Grain boundary (low strain)	526.56	582.11	244.80	90.24	4795.60	4292.29	481.35	457.95	9.23	5.83	3.66	4.93	36.00	2517.69	2253.45

(*continued on next page*)

Table 2 (*continued*)

Sample name	Pressure in GPa (for deformation expts); experimental conditions or type of material	Microstructure	Epoxy organics, total integrated absorbance (cm^{-2})	Standard deviation	AlH total integrated absorbance (cm^{-2})	Standard deviation	H_2O broad total integrated absorbance (cm^{-2})	Standard deviation	Band at 3627 cm^{-1}, total integrated absorbance (cm^{-2}) (assume isotropic)	Standard deviation	Band at 3585 cm^{-1}, total integrated absorbance (cm^{-2})	Standard deviation	Band at 3700 cm^{-1}, total integrated absorbance (cm^{-2}) (assume isotropic)	Standard deviation	Number of measurements	Water concentration in quartz (H/10^6 Si)	Uncertainty (H/10^6 Si)
		Grain interior (high strain)	206.95	308.18	143.31	89.15	2917.04	2425.44	107.71	141.42	17.94	6.21	5.18	6.58	34.00	1531.44	1273.35
		Grain boundary (high strain)	843.89	864.61	303.66	181.66	5457.45	3754.95	215.25	173.78	10.81	4.20	4.22	6.44	45.00	2865.16	1971.35
OR64	1.5	Grain interior (low strain)	297.39	333.72	138.33	95.28	5017.41	3882.62	1199.35	841.40	10.78	5.43	19.09	25.47	30.00	2634.14	2038.38
		Grain boundary (low strain)	477.56	613.61	180.97	104.12	4948.24	3642.34	1976.25	1002.96	5.78	4.05	24.77	34.67	42.00	2597.82	1912.23
		Grain interior (high strain)	470.69	505.03	156.43	91.72	3013.69	2649.25	119.59	104.43	13.86	5.51	5.25	5.39	46.00	1582.19	1390.86
		Grain boundary (high strain)	1576.64	1993.62	252.14	112.26	6098.75	6211.38	266.97	338.87	13.58	5.78	5.04	13.75	48.00	3201.84	3260.98
OR65	2; strain-rate stepping	Grain interior (top)	113.13	105.64	212.59	88.37	3391.98	2310.11	174.35	98.85	17.69	7.64	26.91	19.32	12.00	1780.79	1212.81
		Grain interior (bottom)	315.09	759.13	164.52	52.98	1881.80	1568.64	455.45	474.69	11.76	8.58	0.87	1.54	30.00	987.94	823.54
		Grain interior (middle)	84.19	70.83	191.39	103.63	2886.49	2284.62	129.37	140.68	16.71	5.21	16.99	20.65	16.00	1515.41	1199.42
		Recrystallized grains	315.03	328.64	207.44	89.18	14333.04	6691.62	560.96	296.68	19.92	8.94	17.32	18.78	12.00	7524.85	3513.10
OR66	2; hydrostatic expt	Grain interior (no strain)	112.04	116.43	152.70	88.40	3327.57	3131.96	133.73	153.54	12.06	4.28	2.78	3.45	42.00	1746.97	1644.28
		Grain boundary (no strain)	613.99	688.77	167.38	119.36	5813.92	4376.24	308.27	261.32	14.42	5.23	2.48	5.12	64.00	3052.31	2297.53
OR68	0.8; strain-rate stepping	Grain interior (low strain)	268.74	163.83	204.74	102.19	3312.91	2177.72	394.23	440.97	28.37	12.02	4.42	5.50	51.00	1739.28	1143.30
		Grain boundary (low strain)	1092.45	973.06	254.71	87.86	3737.34	2550.55	1148.08	997.91	12.53	9.28	2.31	4.28	56.00	1962.10	1339.04
		Grain interior (high strain)	190.20	287.69	193.30	86.17	3205.50	2594.50	145.18	212.48	26.78	10.05	2.05	3.15	47.00	1682.89	1362.11
		Grain boundary (high strain)	450.91	636.45	254.26	95.19	4191.94	3136.56	265.99	194.07	19.62	8.82	3.36	5.36	62.00	2200.77	1646.70
OR73	0.8; no water added	Grain interior (low strain)	1321.78	1173.44	243.62	191.76	5021.23	3966.72	166.47	183.30	5.90	4.04	5.89	9.59	54.00	2636.15	2082.53
		Grain boundary (low strain)	2873.25	2110.45	306.97	152.79	6744.11	4682.85	389.65	399.62	7.35	6.19	2.88	4.42	57.00	3540.66	2458.49
		Grain interior (high strain)	2628.40	1911.23	359.47	235.95	6927.94	6650.42	320.67	375.51	6.00	4.67	3.63	5.41	24.00	3637.17	3491.47
		Grain boundary (high strain)	5079.53	2803.75	392.11	286.19	12351.44	11365.19	622.78	760.59	14.21	11.23	7.96	18.43	22.00	6484.51	5966.72

(*continued on next page*)

Table 2 (*continued*)

Sample name	Pressure in GPa (for deformation expts); experimental conditions or type of material	Microstructure	Epoxy organics, total integrated absorbance (cm^{-2})	Standard deviation	AlH total integrated absorbance (cm^{-2})	Standard deviation	H_2O broad total integrated absorbance (cm^{-2})	Standard deviation	Band at 3627 cm^{-1}, total integrated absorbance (cm^{-2}) (assume isotropic)	Standard deviation	Band at 3585 cm^{-1}, total integrated absorbance (cm^{-2})	Standard deviation	Band at 3700 cm^{-1}, total integrated absorbance (cm^{-2}) (assume isotropic)	Standard deviation	Number of measurements	Water concentration in quartz (H/10^6 Si)	Uncertainty (H/10^6 Si)
TQ2	starting material	Grain interior	1627.39	1884.81	259.52	127.21	8727.57	5799.65	835.74	965.91	4.51	5.32	23.24	33.41	111.00	4581.97	3044.82
		Grain boundary	5443.80	3114.10	466.57	237.16	14517.91	6010.52	1653.96	1170.29	4.43	4.75	88.50	88.22	128.00	7621.90	3155.53
		Cement	4822.45	2920.67	634.73	225.92	15641.44	4660.21	1116.87	819.99	5.15	5.14	71.23	74.05	65.00	8211.75	2446.61
		Triple junction	6840.86	3294.39	529.64	217.83	15674.03	5727.28	1681.05	1337.24	5.39	5.40	86.70	74.24	104.00	8228.86	3006.82

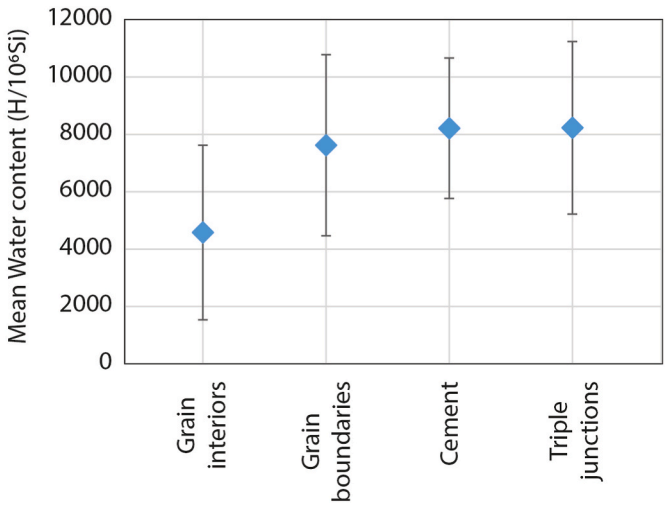

Fig. 3a. Plot of the mean H_2O contents (H/10^6 Si) for the starting material studied (TQ2).

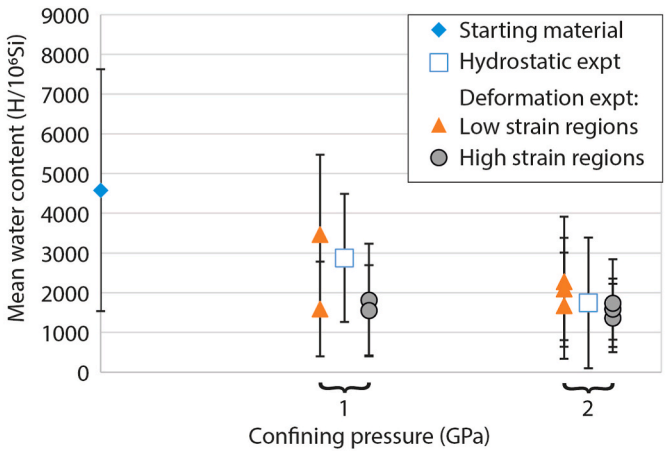

Fig. 3b. Mean H_2O contents (H/10^6 Si) for grain interiors as a function of the confining pressure. H_2O contents of deformed samples are plotted as a range of pressures near the actual pressure of the experiment for the sake of distinguishing them in the representation. In deformed samples low strain and high strain regions are distinguished. The mean H_2O content of deformed and hydrostatically treated samples is substantially reduced compared to the starting material.

conditions on the mean H_2O content of interiors and boundaries of grains (Fig. 3c). The variations in the H_2O content of the starting material, as well as the large uncertainties, make it difficult to interpret subtle inter-sample variations in H_2O content. However, there are significantly higher H_2O contents in grain boundary regions than in grain interiors in all samples, irrespective of applied pressure.

3.4. *Effect of strain on H_2O content*

The effect of deformation on H_2O content was studied in cases where the origin of the starting material samples was known (Fig. 3d). The lower and higher stain regions of an individual sample have been measured, so that the H_2O content is only a function of deformation, not a different H_2O content of the starting material, etc.

The less deformed regions of samples tend to show a higher H_2O content than the more deformed regions (Fig. 3d). The difference between more and less deformed and for grain boundary regions and grain interiors appears to diminish with high confining pressure (2 GPa).

In a series of experiments at 2 GPa different amounts of finite strain

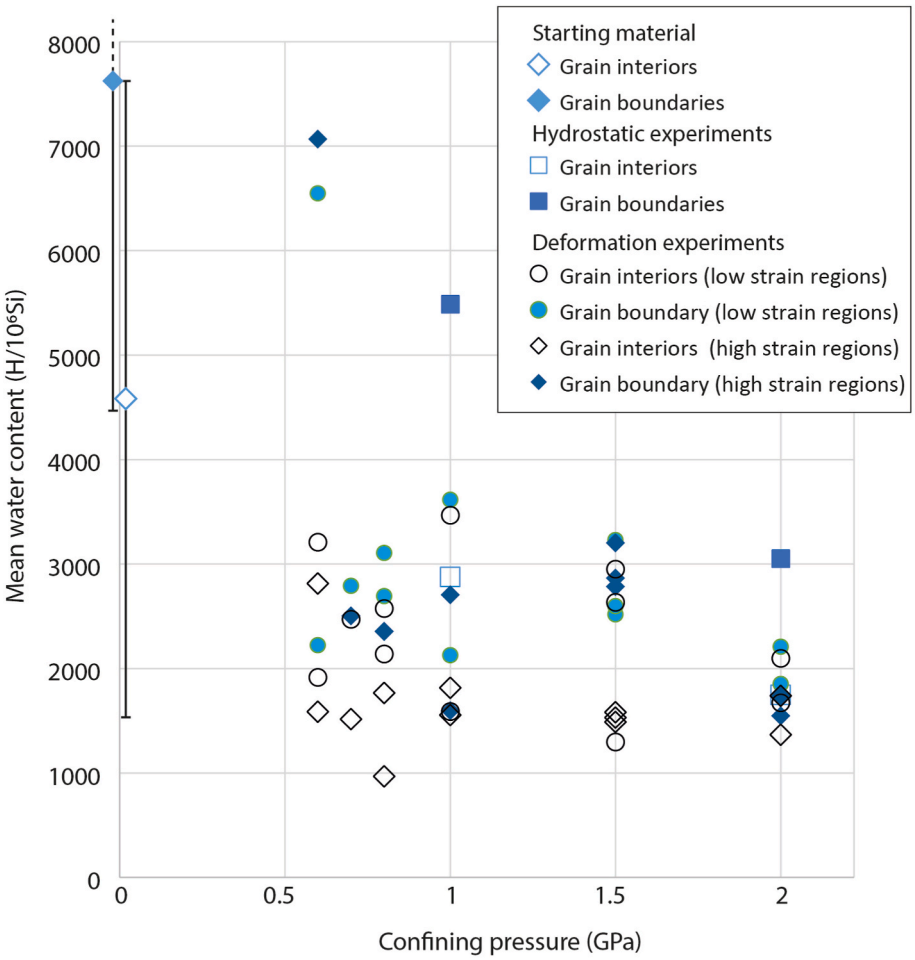

Fig. 3c. Mean H_2O contents ($H/10^6$ Si) for grain interiors and grain boundary regions as a function of the confining pressure for hydrostatic and deformation experiments where bulk strain reached ~30%. In the latter, high strain and low strain regions are distinguished. For the sake of clarity of representation, error bars are not shown.

were achieved. The H_2O content tends to generally decrease with increasing strain, both in the grain interiors and in the grain boundary regions. However, at a higher strain rate, the trend is not obvious (Fig. 3e): the higher strain rate sample shows higher H_2O contents for both, grain interiors and boundary regions.

3.5. Evolution in H_2O content with deformation: a narrowing in the frequency distribution

In the deformed samples, grain interiors and grain boundary regions show a pronounced decrease in values of higher H_2O content and a frequency increase in values of lower H_2O content with respect to the starting material (Fig. 3f) for all measurements. The mode in grain interiors is around 1000–1500 and for grain boundary regions ~1250–1500 $H/10^6$ Si, and the grain boundary region values tend to be more frequent at slightly higher H_2O contents than the grain interiors. There is a clear trend of a pronounced loss of H_2O during deformation compared to the starting material.

3.6. Summary of the distribution of H_2O in the deformed aggregates

Summarizing, the H_2O content in hydrostatically treated and deformed samples is generally higher in the grain boundary region than in grain interiors (Fig. 3). Samples of the starting material already show a trend of this distribution, and the deformed samples show a further decrease in the H_2O content. Generally, the H_2O content evolves towards lower values with increasing deformation (i.e., in Fig. 3f data points tend to shift towards low H_2O contents), but there is no systematic trend for any dependence on confining pressure (Figs. 3c and 4), except that for the highest pressure 2 GPa samples; grain boundary region and grain interior values become indistinguishable (Fig. 4). This situation of H_2O collecting in grain boundary regions is well documented by mapping of the H_2O content (Figs. 5 and 6): After hydrostatic treatment, the H_2O is concentrated in the grain boundary regions (Fig. 5). This development continues after deformation: in the high strain sample OR 56, at high confining pressure, most of the H_2O is located in the larger grain boundary regions of recrystallized grains, i.e., in the domains of recrystallized grains (Fig. 6).

3.7. OH - speciation

The presence of sheet silicates is indicated by the absorption bands in the range of 3625–3700 cm^{-1} in grain boundary regions (Fig. 7) and – to a lesser extent – in grain interiors, too (Fig. 8). Sheet silicates typically occur attached to the surface of the original sand grains, but they do not form a continuous film. During diagenesis, the sheet silicates are overgrown by SiO_2. The sheet silicate content decreases in deformed and hydrostatically treated samples with respect to the starting material or even disappears (due to breakdown of sheet silicates at the high temperature of the experiments; Pongrac et al., 2022). Only some of these absorption bands may persist in a reduced form at high confining pressure conditions.

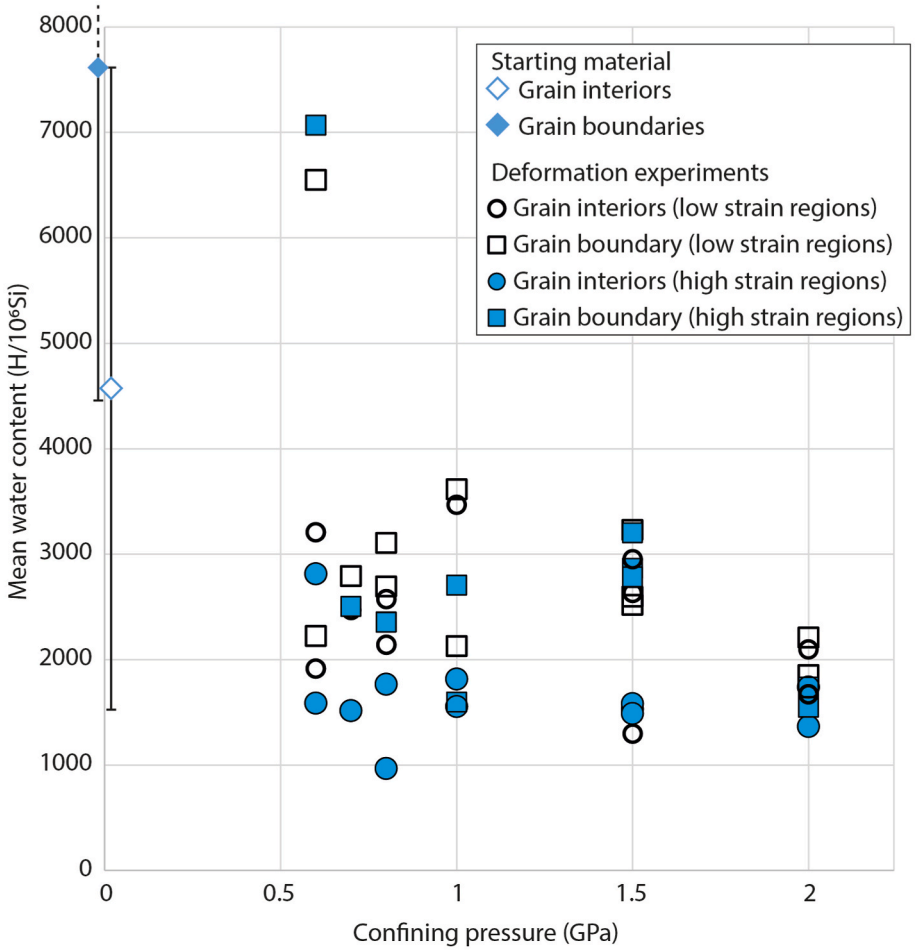

Fig. 3d. Mean H_2O contents (H/10^6 Si) as a function of confining pressure, for high and low strain regions of samples experimentally deformed to bulk strain of ~30%. No connection between mean H_2O contents and confining pressure is observed. Mean H_2O contents tend to decrease with increasing strain. For the sake of clarity of representation, error bars are not shown.

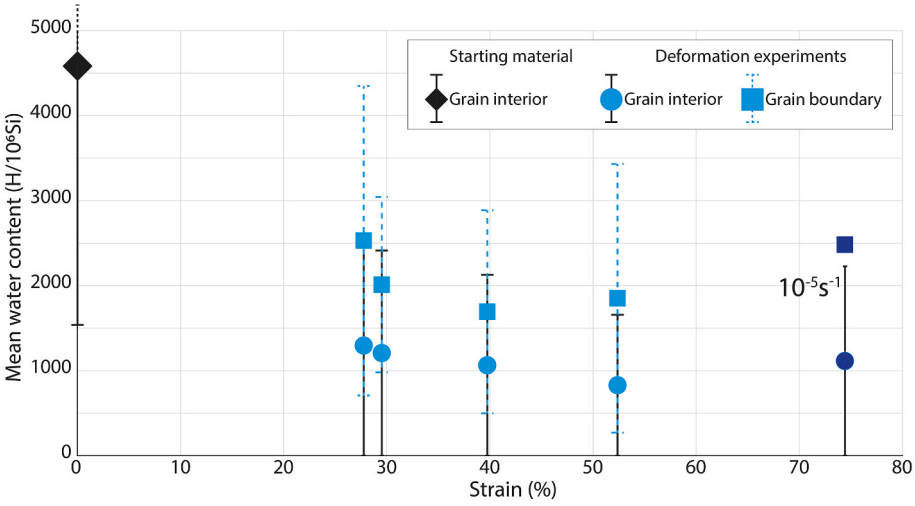

Fig. 3e. Mean H_2O contents (H/10^6 Si) for samples deformed at 2000 MPa (and starting material for comparison) as a function of the global strain achieved. Samples with 27.76–52.38% strain were deformed at 10^{-6} s^{-1} strain rate, whereas the sample with 74.43% strain was deformed at 10^{-5} s^{-1}.

In grain interiors, the 3585 cm^{-1} band starts to appear as a discrete band more frequently than in the starting material above confining pressures of ~700 MPa (Fig. 8) and its absorbance shows a systematic increase with increasing confining pressure (Fig. 9). This trend is also visible in grain boundary regions (Fig. 7).

The Al–H triplet, with peaks at 3317, 3375 and 3438 cm^{-1} discrete absorption bands, tends to become more prominent with deformation and with increasing confining pressure (Fig. 8). It is interesting to note

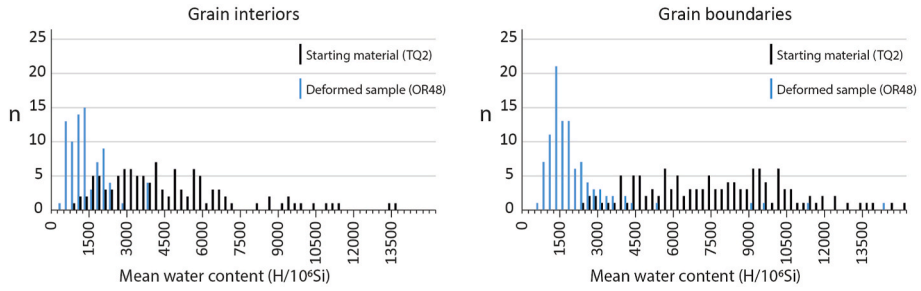

Fig. 3f. Distribution of H_2O contents of individual measurements for grain interiors and grain boundaries (H/10^6 Si) in deformed sample OR48 (1.25 GPa) compared to the starting material TQ2. The H_2O contents of individual measurements in the deformed sample are concentrated at lower values and show less dispersion in H_2O content than the starting material.

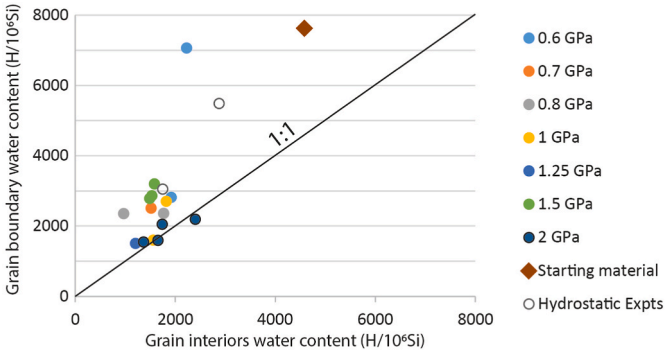

Fig. 4. Relationship between mean grain interior and grain boundary region H_2O contents (H/10^6 Si). The mean H_2O content of grain boundaries is generally higher than the grain interior one, but there is no systematic change with confining pressure, except that the highest pressure (2 GPa) samples plot very near the 1:1 slope.

that the absorbance of the triplet tends to be higher in the grain boundary regions than in grain interiors (Fig. 10). This observation becomes obvious in the FTIR maps (Figs. 5 and 6). The centre absorption band (3375 cm^{-1}) of the three is the most prominent one, being responsible for the pointed nature of the broad H_2O absorption band in deformed samples.

4. Discussion

4.1. H_2O transfer

The H_2O content decreases in deformed and hydrostatically (P, T)-treated samples with respect to the starting material (Fig. 3), and there is more H_2O stored in the grain boundary regions than in grain interiors (Figs. 3 and 4). A reduction in H_2O content in experimental samples after deformation has already been observed by Stipp et al. (2006). The net loss of H_2O from samples may have occurred by H-diffusion through the Pt-jacket into the salt confining medium. Hydrostatic experiments have been carried out for approximately the same duration as the deformation experiments, 252 h at 1 GPa and 217 h at 2 GPa (Table 1). At 2 GPa the H_2O content of the hydrostatic sample is lower after shorter duration than at 1 GPa (Fig. 3b) and longer duration, so that the net loss is not simply time (or diffusion) dependent. Some of the H_2O will fractionate into small amounts of melt (<1 vol %) that collect in small pockets (Négre et al., 2021; Pongrac et al., 2022). Such pockets have been avoided in the FTIR measurements as they do not contain quartz as the main constituent. These melt pockets probably account for substantial amounts of the net H_2O loss measured by FTIR, but loss by diffusion through the jacket cannot be excluded.

The re-distribution of H_2O within the samples is of major interest in this study. Post and Tullis (1998) have demonstrated that H_2O uptake of vacuum-dried quartz grains is very rapid in deformation experiments. A hydration of dry grains to become "wet" and H_2O loss from grains with high H_2O contents to the matrix during experimental deformation has been observed by Palazzin et al. (2018). Thus, transfer of H_2O between quartz grains and a H_2O reservoir is known to occur on the laboratory time scale of deformation experiments. Here, it is observed that differences or transfer of H_2O between grain interiors and the grain boundary regions can take place or is enhanced during deformation and hydrostatic treatment.

The measured OH of the broad absorption band of this study is mainly present as molecular H_2O. Only small quantities (a few ppm H/10^6Si) may be present in the form of structurally bound or point defect OH-contents (Paterson, 1989), e.g., forming the discrete 3585 cm^{-1} absorption band (Jollands et al., 2020, Stünitz et al., 2017). Molecular H_2O is a disequilibrium feature in quartz and the storage of H_2O in quartz is only possible in the form of fluid inclusions (down to nanometric size).

Diffusion of H_2O into quartz is not feasible or too slow on a laboratory time scale (Kronenberg et al., 1986; Gerretsen et al., 1989), so that other processes than diffusion have to account for the transfer of H_2O between the grain interiors and the grain boundary region. The transfer processes typically involve (micro)-cracking (including decrepitation of fluid inclusions) and advective H_2O transport (Kronenberg et al., 1986; Gerretsen et al., 1989; Hall and Sterner, 1993; Vityk and Bodnar, 1995; Schmocker et al., 2003; Tarantola et al., 2012). Traces of the (micro)--fractures may be difficult to detect because of rapid and efficient crack healing in quartz (Hall and Sterner, 1993; Vityk and Bodnar, 1995; Tarantola et al., 2010, 2012). As most of the H_2O is contained in fluid inclusions, the shift towards lower H_2O values in individual measurements indicates a decrepitation of larger fluid inclusions and formation of smaller ones during deformation (e.g., Stünitz et al., 2017). In our samples, it is inferred that decrepitation of fluid inclusions commences during the hydrostatic stage of temperature and pressure treatment before deformation, because hydrostatically treated samples tend to show the strongest decrease in H_2O content in grain interiors with respect to the starting material (Fig. 3). A further H_2O decrease continues to take place in deformed samples (Fig. 3b and c), and individual OH measurements yield lower H_2O contents in deformed samples (Fig. 3f). Increasing strain promotes H_2O loss from grain interiors (Fig. 3d and e), consistent with the observation that (micro)-cracking and crack healing occur during all deformation stages (Tarantola et al., 2010, 2012; Stünitz et al., 2017; Négre et al., 2021; Pongrac et al., 2022), together with plastic deformation of grains. This observation may suggest that pipe diffusion in moving dislocations (Yund et al., 1981) can contribute to H_2O loss in deforming grains as already suspected by Kronenberg et al. (2017, 2020) and Bakker and Jansen (1994).

It should be noted that the grain boundary as a surface between two grains cannot store a sufficient amount of H_2O to account for the total H_2O measured in the grain boundary regions. For a 20 by 50 μm measurement area and a thickness of ~100 μm of the FTIR sections, a grain boundary layer of 2 nm H_2O would correspond to ~250 H/10^6 Si,

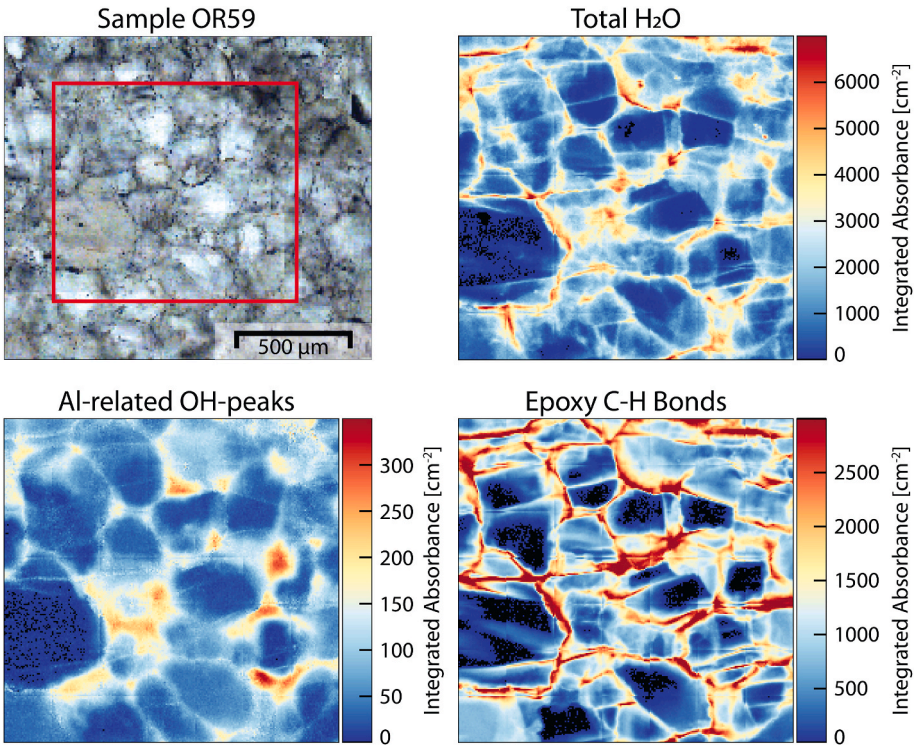

Fig. 5. High resolution transmission FTIR-FPA mapping showing the variation of absorbance and hence the distribution of H_2O content, epoxy C–H bonds and Al-related OH in sample OR59 (1 GPa pressure) within the wavenumber regions of 3050–3600 cm^{-1} (H_2O), 2700-3000 cm^{-1} (epoxy C–H) and 3313-3400 cm^{-1} (Al-related OH). Upper left hand image is a plane polarized light microscope image with the red frame showing the mapped region. After hydrostatic pressure and temperature treatment only (no deformation), most of the H_2O is contained in the grain boundary regions. Note that the absorption of Al-related OH depends on the orientation of the grain. Therefore, absolute values can only be compared directly among grains with the same orientation. However, individual grains consistently show enrichment of Al-related OH in the grain boundary region. (For interpretation of the references to colour in this figure legend, the reader is referred to the web version of this article.)

whereas much higher contents (~1500 to ~3500 H/10^6 Si) are measured (Figs. 3 and 4). Thus, defects (microcracks, dislocations, fluid inclusions, etc.) near the grain boundary are inferred to be the main storage sites for the measured H_2O near the boundaries. We therefore refer to "grain boundary regions" in this study, not only the boundary surface layer itself to include a volume of quartz material immediately adjacent to the boundary.

4.2. Relationship between water content, deformation, and mechanical strength

H_2O weakening in quartz depends on the presence of molecular H_2O (e.g., Kekulawala et al., 1981), which is a disequilibrium effect, because the solubility of H_2O in quartz is extremely small (e.g., Paterson 1986, 1989; Cordier and Doukhan 1989). The disequilibrium nature of the H_2O content in quartz crystals implies that it is not directly dependent on pressure or temperature. Although the mechanical strength of quartz is dependent on the H_2O-content (Griggs and Blacic 1965; Griggs 1967; Jaoul et al., 1984; Doukhan and Trépied 1985; Cordier and Doukhan 1989; Paterson 1989; Tullis and Yund 1989; Hirth and Tullis 1992; Post et al., 1996; Holyoke and Kronenberg 2013), it is difficult to predict or quantify the H_2O weakening effect for a given H_2O content. Given the strength dependence on H_2O content, it might be expected that decreasing H_2O contents in quartz crystals could lead to relative mechanical hardening. However, such an effect is not observed in this study. Post and Tullis (1998) have observed very strong behavior of quartz in dried samples, but these were effectively dry crystals of less than 300 ppm H. In previous studies (Palazzin et al., 2018; Négre et al., 2021; Pongrac et al., 2022), reduced H_2O contents of several hundred ppm H compared to starting contents of more than 1000 ppm H did not produce mechanical hardening. From this study it appears that contents of 1000–3500 ppm H are typical for lower strains in grain interiors at moderate to high pressures, whereas grain boundary regions tend to contain 1500–4000 ppm H (Fig. 3). At higher strain the H_2O contents can decrease to ~700 ppm H without hardening of the samples.

In nature, higher H_2O contents in shear zones than in undeformed host rock have been measured (Kronenberg and Wolf 1990; Kronenberg et al., 1990; Nakashima et al., 1995), but recent studies have shown decreasing H_2O contents during deformation processes in natural shear zones (e.g., Kilian et al., 2016; Kronenberg et al., 2017, 2020; Fukuda et al., 2023) without an indication for hardening of the zones. These results indicate that H_2O contents of natural shear zones can be very variable without a direct indication for the relative mechanical strength of such zones, so that it appears impossible to infer mechanical strength from H_2O contents alone. Comparatively small H_2O contents of several hundred ppm H appear to be sufficient to ensure crystal plastic deformation of quartz in experiments and in nature.

As H_2O contents of the grain boundary regions tend to be higher than in grain interiors. The larger part of H_2O appears to be retained in the samples and is only transferred from interiors to grain boundary regions. The same situation was observed by Kilian et al. (2016) in deformed natural quartz samples: Grain boundary migration had removed aqueous fluid from fluid inclusions in grain interiors to produce very dry grains (<100 ppm H), while hydrous phases have formed in the rock during deformation, indicating that H_2O remained available in the grain boundary regions of the shear zone. The dry quartz grains continue to deform in the natural case, and either such low H_2O contents of <100 ppm H are sufficient to deform quartz plastically or the "dry" state or these low H_2O contents represent a transient state and H_2O is re-introduced into the grains by, e.g., microcracks (Kilian et al., 2016). In the experimentally deformed grains here there is evidence for abundant micro-cracking producing recrystallized grains (Négre et al., 2021;

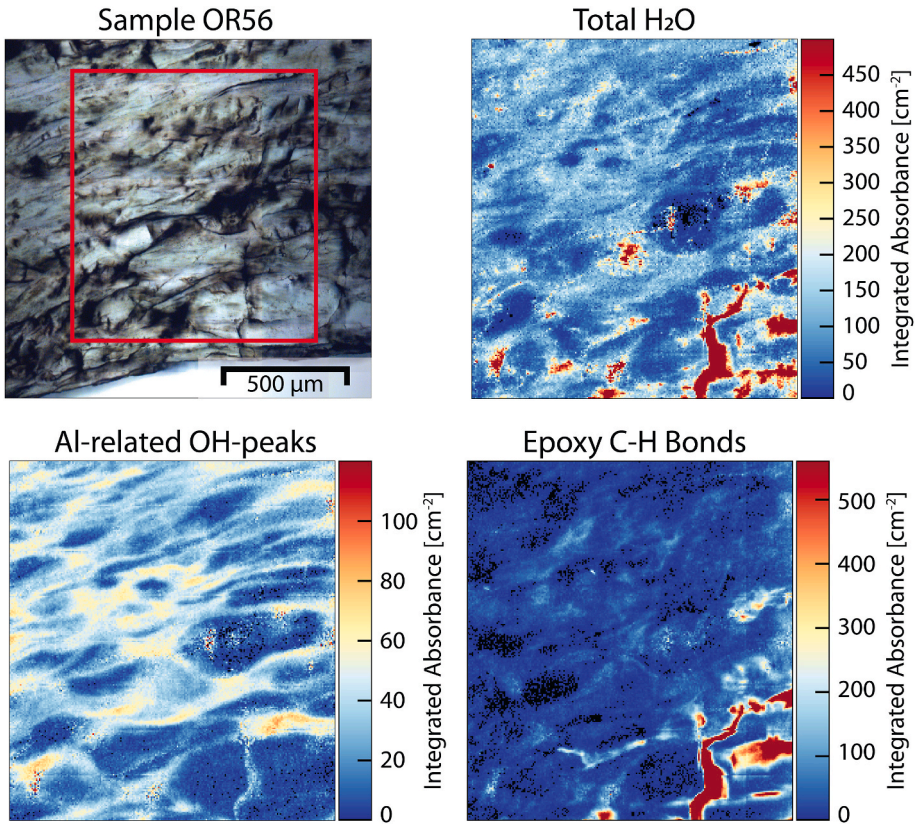

Fig. 6. Mapping of H_2O content, epoxy, and Al in sample OR56 (2 GPa pressure, higher strain rate and high strain) for wave number regions 3050-3600 cm^{-1} (H_2O), 2700-3000 cm^{-1} (epoxy C–H) and 3313-3400 cm^{-1} (Al-related OH). Upper left hand image is a plane polarized light image with the red frame showing the mapped region. Most of the epoxy is contained in cracks (lower right). The grain boundary regions contain most of the H_2O, especially in the domains of recrystallized fine grained quartz regions (upper left region of the image). (For interpretation of the references to colour in this figure legend, the reader is referred to the web version of this article.)

Pongrac et al., 2022). Microcracking and crack healing (Tarantola et al., 2010, 2012; Stünitz et al., 2017; Palazzin et al., 2018) are known to facilitate re-introduction of H_2O into the deforming grains. Thus, it is inferred from this study that the option of re-introducing H_2O back into grains appears a viable and likely process for continued deformation of quartz (even if transiently lower H_2O contents could form), as long as the H_2O remains in the grain boundary regions of the deforming material. If the H_2O content of old grains is only lowered by plastic deformation or microcracking to some degree and not as dramatically as described by Kilian et al. (2016), because no grain boundaries have swept the whole grains, the remaining H_2O is sufficient to facilitate plastic deformation without hardening (as it is the case here).

The absorbance of the 3585 cm^{-1} absorption band increases with increasing confining pressure (Figs. 7–9). This discrete absorption band has been associated with OH stored in dislocations, consistent with observations in natural and synthetic quartz (Stünitz et al., 2017) and molecular simulations indicating an OH- group bridging 2 Si atoms linked by an O-atom (Jollands et al., 2020). A hydrogrossular defect ^{4}H–Si postulated by Stalder and Konzett (2012) for this discrete band might be another possibility for this defect and could still be connected to dislocations. The increased absorbance of the 3585 cm^{-1} band with increasing pressure would either imply an increased OH-content in the dislocations with increased H_2O-fugacity (Henry's law) or an increased dislocation density at higher confining pressure. An increased absorbance of the 3585 cm^{-1} band with increased H_2O fugacity had been predicted by Jollands et al. (2020).

At higher confining pressures the investigated samples deform at lower stresses (Négre et al., 2021), consistent with previous observations (e.g., Kronenberg and Tullis, 1984; Holyoke and Kronenberg 2013). An empirical relationship predicts a higher dislocation density for higher differential stress during dislocation creep (e.g., Karato 2008; Paterson 2013). Thus, one would expect a lower dislocation density at higher confining pressures (because of lower differential stresses) instead of higher dislocation densities. The more prominent absorption by the 3585 cm^{-1} band at higher confining pressure probably is best explained by a larger uptake of OH at the increased H_2O-fugacity at higher pressure (Henry's law). Summarizing the effects of H_2O transfer during deformation it can be inferred that the transfer of H_2O from grain interiors to the grain boundaries does not have a strengthening effect on the deforming material and that H_2O contents of ~700 ppm H are sufficient to ensure a weak rheology of quartz. The transfer or exchange of H_2O will most likely take place by microcracking, even at high P and T, possibly together with transport via dislocations.

4.3. Other chemical exchanges

The absorbance of the triplet at 3317, 3375 and 3438 cm^{-1} (Al–H band): This triplet of absorption bands increases for grain boundaries compared to grain interiors (Figs. 7, 8 and 10). The triplet is assigned to H-content as a charge balance for Al substitution (Kronenberg 1994 (and references therein); Stalder and Konzett, 2012; Jollands et al., 2020). Some of the cathodoluminescence (CL) signals in recrystallized quartz, especially in grain boundary regions of cracked and recrystallized grains, tends to show some spatial relationship with high Al-values (Pongrac et al., 2022). There is a very small amount of melt forming from sheet silicate breakdown at the high temperatures of the experiments (900 °C). Often the high Al-contents are located near small melt pockets. The spatial coincidence may indicate that some Al-exchange took place between melt and quartz grains in the grain boundary regions. More importantly, some grain boundary migration occurs during

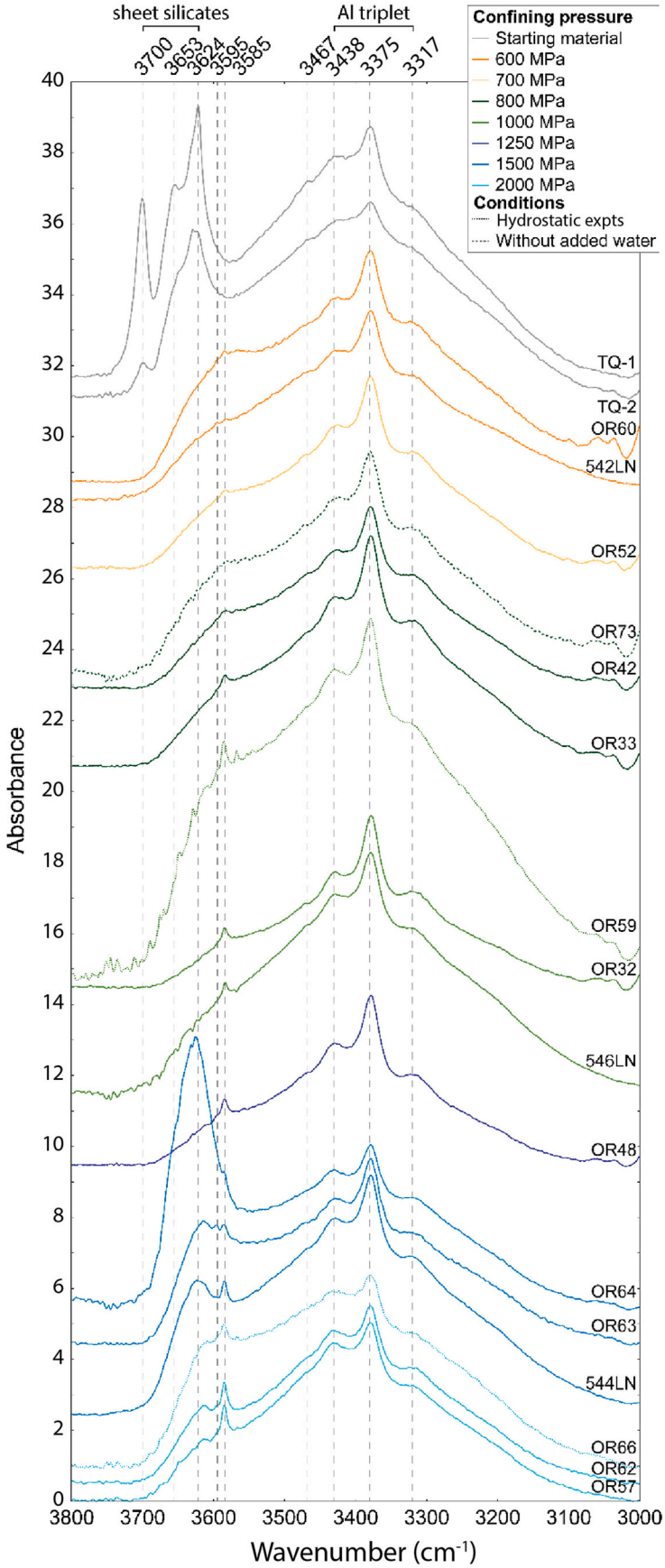

Fig. 7. Average spectra for grain boundaries of starting material, hydrostatic samples, and samples deformed at 10^{-6} s^{-1} at pressures from 600 to 2000 MPa. Spectra are normalized to 1 mm thickness and shifted.

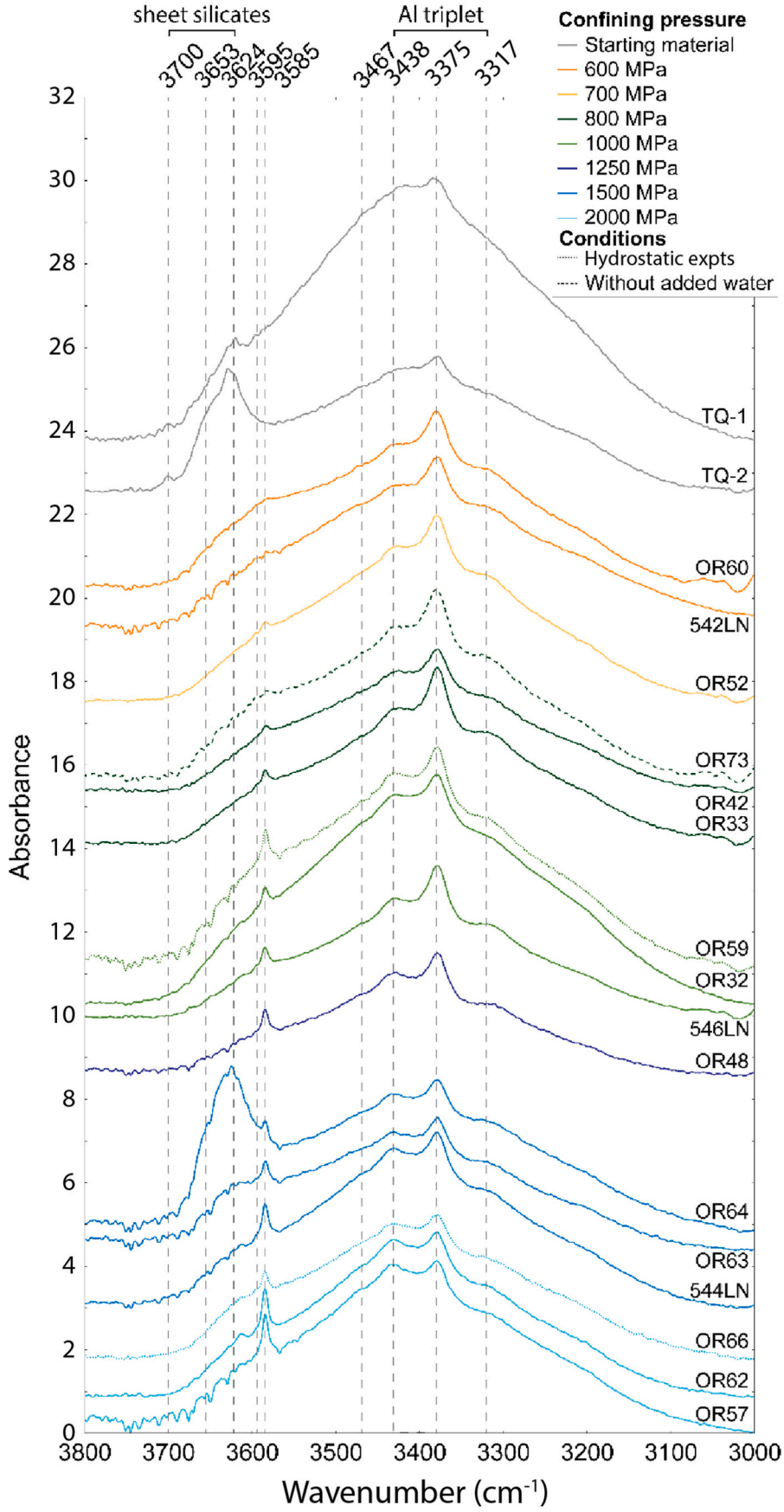

Fig. 8. Average spectra for grain interiors of starting material, hydrostatic samples, and samples deformed at 10^{-6} s^{-1} at pressure from 600 to 2000 MPa. Spectra are normalized to 1 mm thickness and shifted.

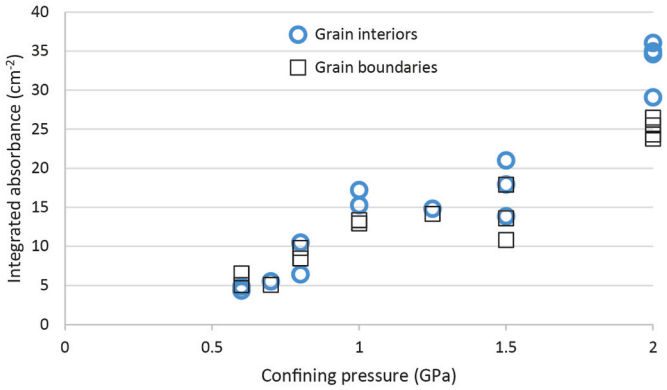

Fig. 9. Total absorbance at 3585 cm^{-1} as a function of the confining pressure. The absorbance of the band increases with pressure. Measurements were carried out in the high strain zones of the experimental samples.

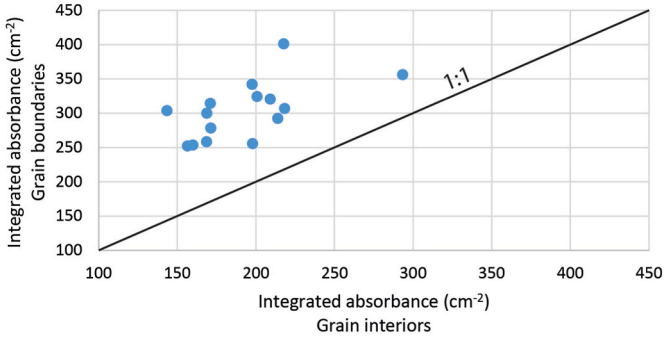

Fig. 10. Total absorbance (integration of the region 3000 to 3800 cm^{-1}) of the Al–H triplet (3317, 3375 and 3438 cm^{-1}) at grain interiors vs. grain boundary regions.

deformation in our samples. Elevated Al-contents produce a different CL-signal that is observed in the grain boundary regions (Pongrac et al., 2022), so that element exchange may be facilitated during grain boundary migration. Enhanced grain boundary migration may be a consequence of enhanced solubility of SiO_2 at higher pressure (e.g., Manning, 1994, 2018), explaining a more pronounced triplet of absorption bands at higher pressures (Figs. 7 and 10).

4.4. Deformation mechanisms

Several recent studies have determined a stress exponent of $n \approx 2$ in quartz deformation experiments (Fukuda et al., 2018; Richter et al., 2018; Négre et al., 2021; Pongrac et al., 2022; Ghosh et al., 2022), concurrent with some earlier observations of similar low n-values (Jaoul et al., 1984; Luan and Paterson, 1992). For climb-controlled dislocation creep the n-value should be approximately between 3 and 5 (Karato 2008; Paterson 2013). The interpretation of the low n-value is given as a combination of dislocation glide/creep and diffusion creep. The relationship between the two deformation mechanisms is not seen as a simple operation of these two mechanisms in parallel, but as a serial process, where the diffusion creep and grain boundary sliding may accommodate strain incompatibilities arising from the operation of less than 5 independent slip systems during dislocation glide (the common situation for quartz). This interpretation is made in analogy to "wet" ice, where a stress exponent of $n = 2$ is observed over a large grain size range (Goldsby and Kohlstedt 2001; Kuiper et al., 2020). "Wet" ice is high temperature ice ($T > -10$ °C), where a liquid water film is present on grain boundaries. This liquid water film accommodates grain boundary sliding and diffusive mass transfer. These latter two processes help to overcome strain incompatibilities and accommodate dislocation creep when less than 5 independent slip systems operate (Goldsby and Kohlstedt 2001; Kuiper et al., 2020). Less than 5 independent slip systems are the normal situation in most silicates, so that strain incompatibilities are an important aspect in silicate dislocation creep. The low stress exponent of $n = 2$ in dislocation creep may be explained by overcoming strain incompatibilities by diffusive mass transfer and grain boundary sliding instead of climb control. The elevated H_2O content in the grain boundary region of deformed quartz aggregates documented in this study may be a similar situation as the liquid H_2O films in "wet" ice. Dissolution-precipitation processes in the grain boundary regions and recrystallized grains have already been inferred for the deforming quartz aggregates (Négre et al., 2021; Pongrac et al., 2022), supporting an analogy to "wet" ice. Higher confining pressures may enhance dissolution rates (Manning 2018) and thus potentially the efficiency of grain boundary processes.

It is interesting to note that the H_2O in the grain boundary regions in this study is partially derived from the grain interiors. Such a situation has already been observed by Kilian et al. (2016) in natural rocks. The ubiquitous abundance of fluid inclusions in quartz grains may provide a typical source for H_2O in quartz deformation. Decrepitation of such inclusions is documented in experimental studies (FitzGerald et al., 1991; Tarantola et al., 2010, 2012; Stünitz et al., 2017) and provides a viable process for the transfer of H_2O from the interiors of grains towards the grain boundaries (cf. Stipp et al., 2006). Microcracking and crack healing are a closely related processes that may transfer the H_2O back into the grain interiors.

4.5. Geological applications – presence and storage of H_2O in mylonites

This study illustrates that the amount of H_2O required for the deformation of quartz is relatively small (~several hundred ppm H). This range of H-contents is similar to that of previous studies (Post and Tullis 1998; Stipp et al., 2006; Gleason and DeSisto, 2008). Natural quartzites like the Tana quartzite used in this study contain far greater amounts of H_2O, so that the local H_2O content may well be reduced substantially without causing a hardening of the deforming quartz due to insufficient H_2O (Kronenberg et al., 2017, 2020; Kilian et al., 2016).

The H_2O lost from the interiors of grains has remained in the grain boundary regions as observed in other studies (Kilian et al., 2016; Kronenberg et al., 2017, 2020). It may be important for the deformation process that this H_2O reservoir in grain boundaries is maintained during the deformation, because it may facilitate dissolution precipitation processes and grain boundary sliding, both of which seem to be important for accommodation processes during dislocation creep. Likewise, dynamic recrystallization is known to be enhanced by H_2O (e.g., Tullis and Yund, 1989). Re-introduction of H_2O into deforming quartz grains (if H_2O loss has been extreme as demonstrated by Kilian et al., 2016) through micro-cracking is very likely, too and dependent on the presence of a H_2O reservoir in grain boundaries.

Grain boundary sliding and cavitation processes are known to maintain aqueous fluids in shear zones (e.g., Fusseis et al., 2009). Thus, it appears likely that H_2O in the grain boundary regions of the deforming aggregate can be retained. However, when temperatures reach conditions of partial melting, the H_2O will partition into the melt, and if the melt is removed from the deforming rock, this process may cause an effective drying of the deforming rock, leading to high stresses during deformation (e.g., Menegon et al., 2011). Such conditions may be realized in the granulite facies, so that strong mechanical behavior of quartz may be expected as a consequence of a vanished grain boundary H_2O reservoir. Thus, maintaining the H_2O budget of the whole rock is important, even if the intracrystalline H_2O content of the quartz grains (transiently) can be small.

5. Conclusions

Detailed measurements of H_2O content by FTIR in very pure Tana quartzite starting material and in experimentally deformed samples of this material at 900 °C and various pressures show that there is a higher H_2O content in the grain boundary regions than in grain interiors in the starting material. This trend is enhanced during hydrostatic treatment and continues further during deformation. The reason for the increasing H_2O content in grain boundaries and decreasing H_2O in grain interiors is inferred to be H_2O transfer from fluid inclusions in the interiors to the grain boundaries by microcracking and advective processes, including potential transport via dislocations. Increasing confining pressure does not show systematic effects on transport, so that the H_2O transfer processes do not appear to be pressure dependent.

The absorbance of the 3585 cm^{-1} absorption band increases systematically with confining pressure. This band is at least in part associated with OH contained in dislocations, so that probably the dislocations can absorb more OH with increasing pressure. The absorbance of the triplet of the Al–H discrete absorption bands becomes systematically higher in grain boundary regions than in grain interiors with deformation. As these absorption bands have been assigned to H incorporated in quartz as a charge balance for Al, it is inferred that there is an Al-exchange of quartz during grain boundary migration or with the very small amount of Al-containing melt generated during the experiments.

The grain boundaries play an important role for facilitating solution precipitation processes for grain boundary migration and grain boundary sliding during continued plastic deformation. H_2O in the experimental samples is not lost during the deformation, so that despite decreasing H_2O in grain interiors samples do not harden. H_2O may be reintroduced into grains from the grain boundary region as long as the H_2O is retained in the sample. It is inferred for natural deformation processes that, as long as H_2O is retained in the grain boundary regions, the internal H_2O content of most natural samples will be sufficient to facilitate quartz deformation. H_2O may be transferred back and forth between grain interiors and grain boundaries through microcracking as long as the grain boundaries act as a fluid reservoir. Low contents of several hundreds of ppm H are sufficient to induce H_2O weakening of quartz.

CRediT authorship contribution statement

H. Stünitz: Conceptualization, Project administration, Supervision, Writing – original draft, Writing – review & editing. **H. Raimbourg:** Conceptualization, Data curation, Formal analysis, Funding acquisition, Investigation, Methodology, Project administration, Supervision, Writing – review & editing. **L. Nègre:** Data curation, Investigation, Methodology. **J. Précigout:** Data curation, Formal analysis, Investigation, Methodology. **M. Jollands:** Data curation, Investigation, Methodology, Software. **P. Pongrac:** Data curation, Investigation. **P. Jeřabek:** Conceptualization, Funding acquisition, Project administration, Writing – review & editing. **N. Gies:** Data curation, Methodology, Software, Validation, Visualization. **M. Lüder:** Data curation, Investigation.

Declaration of competing interest

The authors declare that they have no known competing financial interests or personal relationships that could have appeared to influence the work reported in this paper.

Data availability

Data will be made available on request.

Acknowledgements

Aneta Slodczyk has helped with the FTIR analyses, and Sylvain Janiec has prepared thin and thick sections for this study. Careful and insightful comments by Junichi Fukuda and an anonymous reviewer have helped to improve the manuscript substantially. The authors acknowledge support from both LabEx VOLTAIRE (ANR-10- LABX-100-01) and EquipEx PLANEX (ANR-11-EQPX-0036) projects.

Appendix A. Supplementary data

Supplementary data to this article can be found online at https://doi.org/10.1016/j.jsg.2023.105029.

References

Aasly, K., Malvik, T., Myrhaug, E.H., 2007. Advanced methods to characterize thermal properties of quartz. In: Conf. Paper INFACON 11, Innovations in Ferro Alloy Industry. http://citeseerx.ist.psu.edu/viewdoc/download?doi=10.1.1.607.1094&rep=rep1&type=pdf.

Aines, R.D., Kirby, S.H., Rossman, G.R., 1984. Hydrogen speciation in synthetic quartz. Phys. Chem. Miner. 11, 204–212.

Bakker, R.J., Jansen, J.B.H., 1994. A mechanism for preferential H_2O leakage from fluid inclusions in quartz, based on TEM observations. Contrib. Mineral. Petrol. 116, 7–20. https://doi.org/10.1007/BF00310686.

Blacic, J.D., 1975. Plastic-deformation mechanisms in quartz: the effect of water. Tectonophysics 27, 271–294. https://doi.org/10.1016/0040-1951(75)90021-9.

Cordier, P., Doukhan, J.C., 1989. Water solubility in quartz and its influence on ductility. Eur. J. Mineral 1, 221–237.

Cordier, P., Doukhan, J.C., Ramboz, C., 1994. Influence of dislocations on water leakage from fluid inclusions in quartz: a quantitative reappraisal. Eur. J. Mineral 6, 745–752. https://doi.org/10.1127/ejm/6/6/0745.

Dimanov, A., Dresen, G., 2005. Rheology of synthetic anorthite-diopside aggregates: implications for ductile shear zones. J. Geophys. Res. Solid Earth 110, 1–24. https://doi.org/10.1029/2004JB003431.

Doukhan, J.C., Trépied, L., 1985. Plastic deformation of quartz single crystals. Bull. Miner. 108, 97–123.

FitzGerald, J.D., Boland, J.N., McLaren, A.C., Ord, A., Hobbs, B.E., 1991. Microstructures in water-weakened single crystals of quartz. J. Geophys. Res. Solid Earth 96, 2139. https://doi.org/10.1029/90JB02190.

Fukuda, J., Holyoke, C.W., Kronenberg, A.K., 2018. Deformation of fine-grained quartz aggregates by mixed diffusion and dislocation creep. J. Geophys. Res. Solid Earth 123, 4676–4696. https://doi.org/10.1029/2017JB015133.

Fukuda, J., Shimizu, I., 2019. Water distribution in quartz schists of the Sanbagawa Metamorphic Belt, Japan: infrared spectroscopic mapping and comparison of the calibrations proposed for determining water contents. Earth Planets Space 71, 1–14.

Fukuda, J., Okudaira, T., Ohtomo, Y., 2023. Water release and homogenization by dynamic recrystallization of quartz. Solid Earth 14, 409–424.

Fusseis, F., Regenauer-Lieb, K., Liu, J., Hough, R.M., De Carlo, F., 2009. Creep cavitation can establish a dynamic granular fluid pump in ductile shear zones. Nature 459, 974–977. https://doi.org/10.1038/nature08051.

Gerretsen, J., Paterson, M.S., McLaren, A.C., 1989. The uptake and solubility of water in quartz at elevated pressure and temperature. Phys. Chem. Miner. 16 https://doi.org/10.1007/BF00199553.

Ghosh, S., Stünitz, H., Raimbourg, H., Précigout, J., 2022. Quartz rheology constrained from constant-load experiments: consequences for the strength of the continental crust. Earth Planet Sci. Lett. 597, 117814 https://doi.org/10.1016/j.epsl.2022.117814.

Gies, N.B., Lanari, P., Herrmann, J. 2023. SpecXY - a tool for working with spectroscopic data. Abstr. 19398, Goldschmidt Lyon2023. https://conf.goldschmidt.info/goldschmidt/2023/meetingapp.cgi/paper/19398.

Gleason, G.C., DeSisto, S., 2008. A natural example of crystal-plastic deformation enhancing the incorporation of water into quartz. Tectonophysics 446, 16–30.

Goldsby, D.L., Kohlstedt, D.L., 2001. Superplastic deformation of ice: experimental observations. J. Geophys. Res. Solid Earth 106, 11017–11030. https://doi.org/10.1029/2000JB900336.

Griggs, D.T., Blacic, J.D., 1965. Quartz: anomalous weakness of synthetic crystals. Science 147, 292–295. https://doi.org/10.1126/science.147.3655.292.

Griggs, D., 1967. Hydrolytic weakening of quartz and other silicates. Geophys. J. Roy. Astron. Soc. 14, 19–31. https://doi.org/10.1111/j.1365-246X.1967.tb06218.x.

Hall, D.L., Sterner, S.M., 1993. Preferential water loss from synthetic fluid inclusions. Contrib. Mineral. Petrol. 114, 489–500.

Hirth, G., Tullis, J., 1992. Dislocation creep regimes in quartz aggregates. J. Struct. Geol. 14, 145–159. https://doi.org/10.1016/0191-8141(92)90053-Y.

Holyoke, C.W., Kronenberg, A.K., 2013. Reversible water weakening of quartz. Earth Planet Sci. Lett. 374, 185–190. https://doi.org/10.1016/j.epsl.2013.05.039.

Jaoul, O., Tullis, J., Kronenberg, A.K., 1984. The effect of varying water contents on the creep behavior of Heavitree quartzite. J. Geophys. Res. Solid Earth 89, 4298–4312. https://doi.org/10.1029/JB089iB06p04298.

Jollands, M.C., Blanchard, M., Balan, E., 2020. Structure and theoretical infrared spectra of OH defects in quartz. Eur. J. Mineral 32, 311–323.

Karato, S.I., 2008. Deformation of Earth Materials: an Introduction to the Rheology of Solid Earth. https://doi.org/10.1017/CBO9780511804892.
Kekulawala, K.R.S.S., Paterson, M.S., Boland, J.N., 1981. An experimental study of the role of water in quartz deformation. Geophys. Monogr. 49–60. https://doi.org/10.1029/gm024p0049.
Kilian, R., Heilbronner, R., Holyoke III, C.W., Kronenberg, A.K., Stünitz, H., 2016. Dislocation creep of dry quartz. J. Geophys. Res. Solid Earth 121, 3278–3299.
Kronenberg, A.K., Tullis, J., 1984. Flow strengths of quartz aggregates: grain size and pressure effects due to hydrolytic weakening. J. Geophys. Res. Solid Earth 4281–4297. https://doi.org/10.1029/JB089iB06p04281@10.1002/(ISSN)2169-9356.CHEMDEF1.
Kronenberg, A.K., Kirby, S.H., Aines, R.D., Rossman, G.R., 1986. Solubility and diffusional uptake of hydrogen in quartz at high water pressures: implications for hydrolytic weakening. J. Geophys. Res. Solid Earth 91, 12723–12741. https://doi.org/10.1029/JB091iB12p12723.
Kronenberg, A.K., Segall, P., Wolf, G.H., 1990. Hydrolytic weakening and penetrative deformation within a natural shear zone. Geophys. Monogr. 56, 21–36.
Kronenberg, A.K., Wolf, G.H., 1990. Fourier transform infrared spectroscopy determinations of intragranular water content in quartz-bearing rocks: implications for hydrolytic weakening in the laboratory and within the earth. Tectonophysics 172, 255–271.
Kronenberg, A.K., 1994. Hydrogen speciation and chemical weakening of quartz, silica: physical behavior, geochem. Mater. Appl. 29, 123–176.
Kronenberg, A.K., Hasnan, H.F., Holyoke III, C.W., Law, R.D., Liu, Z., Thomas, J.B., 2017. Synchrotron FTIR imaging of OH in quartz mylonites. Solid Earth 8, 1025–1045.
Kronenberg, A.K., Ashley, K.T., Francsis, M.K., Holyoke III, C.W., Jezek, L., Kronenberg, J.A., Law, R.D., Thomas, J.B., 2020. Water loss during dynamic recrystallization of Moine thrust quartzites, northwest Scotland. Geology 48, 557–561.
Kuiper, E.J.N., De Bresser, J.H.P., Drury, M.R., Eichler, J., Pennock, G.M., Weikusat, I., 2020. Using a composite flow law to model deformation in the NEEM deep ice core, Greenland-Part 2: the role of grain size and premelting on ice deformation at high homologous temperature. Cryosphere 14. https://doi.org/10.5194/tc-14-2449-2020.
Luan, F.C., Paterson, M.S., 1992. Preparation and deformation of synthetic aggregates of quartz. J. Geophys. Res. Solid Earth 97, 301–320. https://doi.org/10.1029/91JB01748.
Manning, C.E., 1994. The solubility of quartz in H_2O in the lower crust and upper mantle. Geochem. Cosmochim. Acta 58, 4831–4839. https://doi.org/10.1016/0016-7037(94)90214-3.
Manning, C.E., 2018. Fluids of the deep crust: deep is different. Annu. Rev. Earth Planet Sci. 46, 67–97. https://doi.org/10.1146/annurev-earth-060614-105224.
McLaren, A.C., Fitz Gerald, J.D., Gerretsen, J., 1989. Dislocation nucleation and multiplication in synthetic quartz: relevance to water weakening. Phys. Chem. Miner. 16 https://doi.org/10.1007/BF00197016.
Mei, S., Kohlstedt, D.L., 2000. Influence of water on plastic deformation of olivine aggregates: 2. Dislocation creep regime. J. Geophys. Res. Solid Earth 105-B9, 21471–21481.
Menegon, L., Nasipuri, P., Stünitz, H., Behrens, H., Ravna, E., 2011. Dry and strong quartz during deformation of the lower crust in the presence of melt. J. Geophys. Res. Solid Earth 116. https://doi.org/10.1029/2011JB008371.
Nakashima, S., Matayoshi, H., Yuko, T., Michibayashi, K., Masuda, T., Kuroki, N., Yamagashi, H., Ito, Y., Nakamura, A., 1995. Infrared microspectroscopy analysis of water distribution in deformed and metamorphosed rocks. Tectonophysics 245, 263–276.
Négre, L., Stünitz, H., Raimbourg, H., Lee, A., Précigout, J., Pongrac, P., Jeřabek, P., 2021. Effect of pressure on the deformation of quartz aggregates in the presence of H_2O. J. Struct. Geol. 148 https://doi.org/10.1016/j.jsg.2021.104351.
Palazzin, G., Raimbourg, H., Stünitz, H., Heilbronner, R., Neufeld, K., Précigout, J., 2018. Evolution in H_2O contents during deformation of polycrystalline quartz: an experimental study. J. Struct. Geol. 114, 95–110. https://doi.org/10.1016/j.jsg.2018.05.021.
Paterson, M.S., 1982. The determination of hydroxyl by infrared absorption in quartz, silicate glasses and similar materials. Bull. Mineral. 105, 20–29.
Paterson, M.S., 1986. The thermodynamics of water in quartz. Phys. Chem. Miner. 13 (4), 245–255.
Paterson, M.S., 1989. The interaction of water with quartz and its influence in dislocation flow: an overview. Rheol. Solids Earth 107–142.
Paterson, M.S., 2013. Materials Science for Structural Geology. Springer, Dordrecht. https://doi.org/10.1007/978-94-007-5545-1.
Pevik, J.A., 2015. Geological and Mineralogical Characterization of the Upper Part of the Gamasfjell Quartzite at the Vaggecearu Mountain. MSc thesis. NTNU Trondheim, p. 132.
Pongrac, P., Jeřabek, P., Stünitz, H., Raimbourg, H., Heilbronner, R., Racek, M., Nègre, L., 2022. Mechanical properties and recrystallization of quartz in presence of H_2O: combination of cracking, subgrain rotation and dissolution-precipitation processes. J. Struct. Geol. 160 https://doi.org/10.1016/j.jsg.2022.104630.
Post, A.D., Tullis, J., Yund, R.A., 1996. Effects of chemical environment on dislocation creep of quartzite. J. Geophys. Res. Solid Earth 101, 22143–22155. https://doi.org/10.1029/96JB01926.
Post, A., Tullis, J., 1998. The rate of water penetration in experimentally deformed quartzite: implications for hydrolytic weakening. Tectonophysics 295, 117–137.
Précigout, J., Stünitz, H., Pinquier, Y., Champallier, R., Schubnel, A., 2018. High-pressure, high-temperature deformation experiment using the new generation Griggs-type apparatus. J. Vis. Exp. 134, e56841, 10.3791/56841.
Richter, B., Stünitz, H., Heilbronner, R., 2018. The brittle-to-viscous transition in polycrystalline quartz: an experimental study. J. Struct. Geol. 114, 1–21. https://doi.org/10.1016/j.jsg.2018.06.005.
Rybacki, E., Dresen, G., 2000. Dislocation and diffusion creep of synthetic anorthite aggregates. J. Geophys. Res. Solid Earth 105-B11, 26017–26036.
Sambridge, M., FitzGerald, J., Kovacs, I., O'Neill, H.S.C., Hermann, J., 2008. Quantitative absorbance spectroscopy with unpolarized light: Part 1. Physical and mathematical development. Am. Mineral. 93, 751–764. https://doi.org/10.2138/am.2008.2657.
Schmocker, M., Bystricky, M., Kunze, K., Burlini, L., Stünitz, H., Burg, J.P., 2003. Granular flow and Riedel band formation in water-rich quartz aggregates experimentally deformed in torsion. J. Geophys. Res. Solid Earth 108. https://doi.org/10.1029/2002jb001958.
Stalder, R., 2021. OH point defects in quartz–a review. Eur. J. Mineral 33, 145–163.
Stalder, R., Konzett, J., 2012. OH defects in quartz in the system quartz–albite–water and granite–water between 5 and 25 kbar. Phys. Chem. Miner. 39, 817–827.
Stipp, M., Tullis, J., Behrens, H., 2006. Effect of water on the dislocation creep microstructure and flow stress of quartz and implications for the recrystallized grain size piezometer. J. Geophys. Res. Solid Earth 111. https://doi.org/10.1029/2005JB003852.
Stünitz, H., Thust, A., Heilbronner, R., Behrens, H., Kilian, R., Tarantola, A., Gerald, J.D. F., 2017. Water redistribution in experimentally deformed natural milky quartz single crystals—implications for H_2O-weakening processes. J. Geophys. Res. Solid Earth 122, 866–894. https://doi.org/10.1002/2016JB013533.
Tarantola, A., Diamond, L.W., Stünitz, H., 2010. Modification of fluid inclusions in quartz by deviatoric stress I: experimentally induced changes in inclusion shapes and microstructures. Contrib. Mineral. Petrol. 160, 825–843. https://doi.org/10.1007/s00410-010-0509-z.
Tarantola, A., Diamond, L.W., Stünitz, H., Thust, A., Pec, M., 2012. Modification of fluid inclusions in quartz by deviatoric stress. III: influence of principal stresses on inclusion density and orientation. Contrib. Mineral. Petrol. 164, 537–550. https://doi.org/10.1007/s00410-012-0749-1.
Thomas, S.-M., Koch-Müller, M., Reichart, P., Rhede, D., Thomas, R., Wirth, R., Matsyuk, S., 2009. IR calibrations for water determination in olivine, r-GeO_2, and SiO_2 polymorphs. Phys. Chem. Miner. 36, 489–509.
Tullis, J., Yund, R.A., 1980. Hydrolytic weakening of experimentally deformed Westerly granite and Hale albite rock. J. Struct. Geol. 2, 439–451.
Tullis, J., Yund, R.A., 1989. Hydrolytic weakening of quartz aggregates: the effects of water and pressure on recovery. Geophys. Res. Lett. 16, 1343–1346. https://doi.org/10.1029/GL016i011p01343.
Vityk, M.O., Bodnar, R.J., 1995. Textural evolution of synthetic fluid inclusions in quartz during re-equilibration, with applications to tectonic reconstruction. Contrib. Mineral. Petrol. 121, 309–323.
Yund, R.A., Smith, B.M., Tullis, J., 1981. Dislocation-assisted diffusion of oxygen in albite. Phys. Chem. Miner. 7, 185–189.